OVRO-LWA Memo No. 18

Polarization Calibration of solar data recorded with the Owens Valley Radio Observatory's Long Wavelength Array

Surajit Mondal
New Jersey Institute of Technology
September 1, 2025

Submitted 2025 September 2

To cite this memo in another document, use:
"OVRO-LWA Memo 16, 2015 Oct 20, http://tauceti.caltech.edu/LWA/lwamemos.html "

Polarization Calibration of solar data recorded with the Owens Valley Radio Observatory's Long Wavelength Array

Surajit Mondal

September 1, 2025

1 Calibration formalism

1.1 Formalism of calibration using solar beamforming data

During beamforming, the signals from all antennas, after applying the relevant delays and amplitude gain solutions obtained from bandpass calibration, are added. No polarization relevant calibration is applied, by default, before combining the signals[1]. Hence additional calibration is required to calibrate the polarization properties of the observed beamformed signal. However, since the beamformed signal has been obtained by adding over data from all antennas, antenna-dependent terms can not be solved. Hence, the procedure outlined here will only be used to solve for array-averaged quantities. We also assume that the polarization-relevant terms, contributed by the signal chain of the system, is very small. However it must be noted that this is not an additional assumption made during polarization calibration. We have already made this assumption during bandpass calibration, where we have ignored the cross-hand visibilities.

In the linear basis, the relation between the observed beamformed data and the true source model can be written as follows

$$\begin{aligned} \begin{pmatrix} I^{obs}+Q^{obs} & U^{obs}+iV^{obs} \\ U^{obs}-iV^{obs} & I^{obs}-Q^{obs} \end{pmatrix} &= JBSB^{\dagger}J^{\dagger} \\ S &= \begin{pmatrix} I^{model}+Q^{model} & U^{model}+iV^{model} \\ U^{model}-iV^{model} & I^{model}-Q^{model} \end{pmatrix} \end{aligned} \tag{1}$$

Here we have denoted the observed and true Stokes parameters of the sources using superscripts *obs* and *model* respectively. Let us also use a superscript *beam* to denote the elements of the matrix $BSB^{\dagger}$. Thus,

$$\begin{pmatrix} I^{beam}+Q^{beam} & U^{beam}+iV^{beam} \\ U^{beam}-iV^{beam} & I^{beam}-Q^{beam} \end{pmatrix} = BSB^{\dagger} \tag{2}$$

Here B is a 2×2 matrix, which incorporates all the direction-dependent properties of the system. It is related to the primary beam of the antenna. The B matrix is obtained using independent modelling techniques. The direction-independent properties are incorporated in the J matrix, which is another 2×2 matrix. Since beamforming is done towards a single source, which almost always has size much smaller than the primary beam of the instrument, B boils down to a constant 2×2 matrix with values, relevant towards the direction of the source. For a dipole instrument like OVRO-LWA, the B matrix will depend on the altitude and azimuth of the source, and hence can change with time, as the apparent position of the source in the sky changes. J matrix on the other hand is direction independent, and originates from the signal chain of the system. Hence it is expected to be very stable with time.

Any 2×2 matrix can be decomposed into the product of a complex number, unit determinant hermitian matrix, and a unit determinant unitary matrix. Thus,

$$\begin{aligned} J &= xHR = xR\tilde{H} \\ H &= H^{\dagger} \\ \tilde{H} &= \tilde{H}^{\dagger} \\ RR^{\dagger} &= I \\ det(H) &= 1 \\ det(\tilde{H}) &= 1 \\ det(R) &= 1 \end{aligned} \tag{3}$$

An important thing to note that if the order of the Hermitian and Unitary matrices are reversed, then the unitary matrix remains unchanged. Since the bandpass and fluxscale calibration is already applied to the antenna signals before beamforming, we can set $x=1$ and parametrize H as

$$H = \begin{pmatrix} 1 & p \\ p^{*} & 1 \end{pmatrix} \tag{4}$$

[1] We show later that we can apply some precomputed parameters, which are then applied to the signal of each antenna before combining them to form a beamformed data product.

According to Hamaker (2000), H matrix, in general, is responsible for mixing between the following Stokes pairs (I,Q), (I,U) and (I,V). However with the form of H chosen in equation 4, the mixing only happens between (I,U) and (I,V). The R matrix is responsible for the mixing between the Stokes pairs (U,V), (Q,V) and (U,Q). We only consider the mixing in the pair (U,V), which is related to the crosshand phase. The contribution of the signal chain into the mixing of (Q,V) is expected to very minimal due to the excellent isolation of the two polarization signals. We mixing between (U,Q) is a coordinate transformation between the antenna coordinate frame and the astronomical coordinate system. This can be represented as a rotation and is incorporated into the B matrix. Hence, we can parametrize R using a parameter δ, referred as the crosshand phase.

$$R = \begin{pmatrix} e^{i\delta} & 0 \\ 0 & 1 \end{pmatrix} \tag{5}$$

The calibration algorithm becomes easier to express in the Stokes basis. So we now do a coordinate transformation of equation 1 to convert to the Stokes basis.

$$\begin{aligned} \begin{pmatrix} I^{obs} \\ Q^{obs} \\ U^{obs} \\ V^{obs} \end{pmatrix} =& TJ \circledast J^{\dagger} P \begin{pmatrix} I^{beam} \\ Q^{beam} \\ U^{beam} \\ V^{beam} \end{pmatrix} \\ T =& \frac{1}{2} \begin{pmatrix} 1 & 0 & 0 & 1 \\ 1 & 0 & 0 & -1 \\ 0 & 1 & 1 & 0 \\ 0 & -i & i & 0 \end{pmatrix}, P = \begin{pmatrix} 1 & 1 & 0 & 0 \\ 0 & 0 & 1 & i \\ 0 & 0 & 1 & -i \\ 1 & -1 & 0 & 0 \end{pmatrix} \end{aligned} \tag{6}$$

By combining equations 4, 5 and 6 we get

$$\begin{pmatrix} I^{obs} \\ Q^{obs} \\ U^{obs} \\ V^{obs} \end{pmatrix} = \begin{pmatrix} 1 & 0 & 0 & 0 \\ 0 & 1 & 0 & 0 \\ 2Real(p) & 0 & \cos\delta & -\sin\delta \\ 2Im(p) & 0 & \sin\delta & \cos\delta \end{pmatrix} \begin{pmatrix} I^{beam} \\ Q^{beam} \\ U^{beam} \\ V^{beam} \end{pmatrix} \tag{7}$$

Now let us also write $(I^{beam}, Q^{beam}, U^{beam}, V^{beam})$ in terms of the expanded B matrix.

$$\begin{pmatrix} I^{beam} \\ Q^{beam} \\ U^{beam} \\ V^{beam} \end{pmatrix} = B \circledast B^{\dagger} \begin{pmatrix} I^{model} \\ Q^{model} \\ U^{model} \\ V^{model} \end{pmatrix} = M \begin{pmatrix} I^{model} \\ Q^{model} \\ U^{model} \\ V^{model} \end{pmatrix} = \begin{pmatrix} M_{00} & M_{01} & M_{02} & M_{03} \\ M_{10} & M_{11} & M_{12} & M_{13} \\ M_{20} & M_{21} & M_{22} & M_{23} \\ M_{30} & M_{31} & M_{32} & M_{33} \end{pmatrix} \begin{pmatrix} I^{model} \\ Q^{model} \\ U^{model} \\ V^{model} \end{pmatrix} \tag{8}$$

In absence of very bright coherent radio bursts, the total flux density of the Sun at all Stokes is dominated by the integrated flux density of the quiet Sun. However, the integrated quiet Sun is expected to be unpolarized. Hence for quiet Sun, $U^{beam} = M_{20} I^{model}$, $V^{beam} = M_{30} I^{model}$. Coherent bursts, however, can have strong circular polarization. However if $M_{20} >> M_{23} f_V$, where f_V is the degree of circular polarization of the coherent radio source, then also, $U^{beam} = M_{20} I^{model} + M_{22} U^{model}$. Similarly if $M_{30} >> M_{32} f_U$, then we can write $V^{beam} = M_{30} I^{model} + M_{33} V^{model}$. We also assume that $M_{0i}/M_{00} << 1$, $i = 1, 2, 3$. Under this assumption, we can write

$$I_{obs} = M_{00} I^{model} \tag{9}$$

$$U^{obs} = 2Real(p) M_{00} I^{model} + (M_{20} I^{model} + M_{22} U^{model}) \cos\delta - (M_{30} I^{model} + M_{33} V^{model}) \sin\delta \tag{10}$$

$$V^{obs} = 2Im(p) M_{00} I^{model} + (M_{20} I^{model} + M_{22} U^{model}) \sin\delta + (M_{30} I^{model} + M_{33} V^{model}) \cos\delta \tag{11}$$

We can rearrange equations 10 and 11 to obtain

$$M_{22} U^{model} + M_{20} I^{model} = \left[U^{obs} - 2Real(p) M_{00} I^{model}\right] \cos\delta + \left[V^{obs} - 2Im(p) M_{00} I^{model}\right] \sin\delta \tag{12}$$

A priori, we do not know the value of p. However, we can replace $2Real(p)$ and $2Im(p)$ by $< U^{obs}/I^{obs} - M_{20}/M_{00} >$ and $< V^{obs}/I^{obs} - M_{30}/M_{00} >$, as long as the data over which the average has been taken corresponds to the quiet Sun. This works because of the fact that the total integrated flux density of the quiet Sun is zero. Thus, we can then rewrite equation 12 as

$$M_{22} U^{model} = \left[U^{obs} - \left\langle \frac{U^{obs}}{I^{obs}} - \frac{M_{20}}{M_{00}} \right\rangle I^{obs}\right] \cos\delta + \left[V^{obs} - \left\langle \frac{V^{obs}}{I^{obs}} - \frac{M_{30}}{M_{00}} \right\rangle I^{obs}\right] \sin\delta - \frac{M_{20}}{M_{00}} I^{obs} \tag{13}$$

Although Dey et al. (2025) have recently shown that coherent radio bursts from the Sun can have linear polarization, we assume that $U^{model} = 0$. Under this assumption, we can solve for δ by minimizing equation 13. While this assumption of $U^{model} = 0$, can lead to incorrect calibration solutions, we discuss later, why this will not cause large errors for the data we have chosen for calibration. While, in principle, we can apply equation 13 to a single time-frequency observation and determine crosshand phase, to increase the accuracy and robustness of solutions, we minimize the sum of $M_{22} U^{model}(t)$ for all times in the dataset. Thus the actual minimization equation we use to determine crosshand phase is

$$\sum_i M_{22}(t_i)U^{model}(t_i) = \sum_i \Bigg\{ \left[U^{obs}(t_i) - \left\langle \frac{U^{obs}}{I^{obs}} - \frac{M_{20}}{M_{00}} \right\rangle I^{obs}(t_i) \right] \cos\delta + \left[V^{obs}(t_i) - \left\langle \frac{V^{obs}}{I^{obs}} - \frac{M_{30}}{M_{00}} \right\rangle I^{obs}(t_i) \right] \sin\delta - \frac{M_{20}(t_i)}{M_{00}(t_i)} I^{obs}(t_i) \Bigg\} \tag{14}$$

We note here that, if $\delta = \delta_0$ minimizes equation 14, $\delta = \delta_0 + \pi$ will also minimize the equation. The π degeneracy is equivalent to reversing the sign of Stokes V. While sources with known Stokes V signs can be used to break this degeneracy, the sky is practically unpolarized at these observation frequencies, which creates an issue in making this possible.

Thus, following the above formalism and under the stated assumptions, we can solve for both p, δ. By combining these parameters with independently available B matrix, we can determine the full Stokes flux density of the Sun. However, in practice, we find that there can be significant errors in the currently available primary beam model. Correcting for the errors in all terms of the primary beam model is very challenging and we do not attempt to do that here. We have only focussed on correcting errors in M_{10}, M_{20}, and M_{30}. However, note that before this step, we have already determined δ by minimizing equation 14. Additionally, let us denote the true values of M_{10}, M_{20}, M_{30} as

$$M_{10} = \tilde{M_{10}} + M_{00}\Delta M_{10} \tag{15}$$
$$M_{20} = \tilde{M_{20}} + M_{00}\Delta M_{20} \tag{16}$$
$$M_{30} = \tilde{M_{30}} + M_{00}\Delta M_{30} \tag{17}$$

$\tilde{M_{10}}, \tilde{M_{20}}, \tilde{M_{30}}$ are the values obtained from the model primary beam. Let us rearrange equation 14 and write

$$U^{obs,crosshand} = U^{obs}\cos\delta + V^{obs}\sin\delta = I^{obs}\left[2Real(p)\cos\delta + 2Im(p)\sin\delta + \frac{\tilde{M_{20}}}{M_{00}} + \Delta M_{20} \right] \tag{18}$$

$$\implies U^{obs,crosshand} - \frac{\tilde{M_{20}}}{M_{00}} I^{obs} = I^{obs}\left[2Real(p)\cos\delta + 2Im(p)\sin\delta + \Delta M_{20} \right] = \alpha_U I^{obs} \tag{19}$$

$$\alpha_U = \left[2Real(p)\cos\delta + 2Im(p)\sin\delta + \Delta M_{20} \right] \tag{20}$$

Similar equations for $Q^{obs,crosshand}, U^{obs,crosshand}$ can also be written.

$$Q^{obs,crosshand} - \frac{\tilde{M_{10}}}{M_{00}} I^{obs} = I^{obs}\Delta M_{10} = \alpha_Q I^{obs} \tag{21}$$

$$\alpha_Q = \Delta M_{10} \tag{22}$$

$$V^{obs,crosshand} - \frac{\tilde{M_{30}}}{M_{00}} I^{obs} = I^{obs}\left[-2Real(p)\sin\delta + 2Im(p)\cos\delta + \Delta M_{30} \right] = \alpha_V I^{obs} \tag{23}$$

$$\alpha_V = \left[-2Real(p)\sin\delta + 2Im(p)\cos\delta + \Delta M_{30} \right] \tag{24}$$

The right hand side of equations 20, 22 and 24 should be direction independent and very stable in time if $\Delta M_{10} = \Delta M_{20} = \Delta M_{30} = 0$. We do a low-order polynomial fit to each of $Q^{obs,crosshand}/I^{obs}$, $U^{obs,crosshand}/I^{obs}$ and $V^{obs,crosshand}/I^{obs}$ and determine $\alpha_Q, \alpha_U, \alpha_V$. While in principle, we can determine p using these equations and data over long time intervals, we do not need to do this. We can determine the cumulative Muller Matrix which takes into account both the effect of the H matrix as well as the B matrix by writing

$$M = \begin{pmatrix} \tilde{M_{00}} & \tilde{M_{01}} & \tilde{M_{02}} & \tilde{M_{03}} \\ \tilde{M_{10}} + \alpha_Q & \tilde{M_{11}} & \tilde{M_{12}} & \tilde{M_{13}} \\ \tilde{M_{20}} + \alpha_U & \tilde{M_{21}} & \tilde{M_{22}} & \tilde{M_{23}} \\ \tilde{M_{30}} + \alpha_V & \tilde{M_{31}} & \tilde{M_{32}} & \tilde{M_{33}} \end{pmatrix} \tag{25}$$

The quantities with tilde are obtained from the model. Then the final polarization calibrated flux densities are

$$\begin{pmatrix} I^{calibrated} \\ Q^{calibrated} \\ U^{calibrated} \\ V^{calibrated} \end{pmatrix} = M^{-1} \begin{pmatrix} I^{obs,crosshand} \\ Q^{obs,crosshand} \\ U^{obs,crosshand} \\ V^{obs_crosshand} \end{pmatrix} = M^{-1} \begin{pmatrix} I^{obs} \\ Q^{obs} \\ U^{obs}\cos\delta + V^{obs}\sin\delta \\ -U^{obs}\sin\delta + V^{obs}\cos\delta \end{pmatrix} \tag{26}$$

1.2 Formalism of calibration using imaging data from astronomical sources and Sun

Polarization calibration using astronomical sources is well developed. Interferometric arrays are able to derive polarization parameters for each antenna using observations of well-modelled astronomical sources called calibrators. As described in Kansabanik et al. (2025), for dipole instruments like OVRO-LWA, having an accurate primary beam model is critical for

such a detailed calibration. However, as discussed in Section 1.1 and 3.1, the primary beam currently available is not very accurate. However, we demonstrate here that in spite of these issues, we can develop calibration schemes with some approximations, which can then be used in solar imaging as well as astronomical imaging, provided certain conditions are satisfied. Below we develop the formalism of this procedure.

This procedure shares a lot of similarity with the calibration procedure described in Section 1.1. To apply a similar procedure, we first synthesize a beamforming data phased on an astronomical source from bandpass calibrated visibility data, using the relations

$$\begin{aligned} P^{XX} =& \frac{1}{\sum_{i\neq j}} \left[\sum_{i\neq j} V_{ij}^{XX} e^{-2\pi i\nu\Delta_{ij}(t)}\right]^2, \; P^{XY} = \frac{1}{\sum_{i\neq j}} \left[\sum_{i\neq j} V_{ij}^{XY} e^{-2\pi i\nu\Delta_{ij}(t)}\right]^2, \\ P^{YX} =& \frac{1}{\sum_{i\neq j}} \left[\sum_{i\neq j} V_{ij}^{YX} e^{-2\pi i\nu\Delta_{ij}(t)}\right]^2, \; P^{YY} = \frac{1}{\sum_{i\neq j}} \left[\sum_{i\neq j} V_{ij}^{YY} e^{-2\pi i\nu\Delta_{ij}(t)}\right]^2 \end{aligned} \tag{27}$$

$P^{XX}, P^{XY}, P^{YX}, P^{YY}$ is the power observed in XX, XY, YX, YY polarization respectively, similar to observed in a beamforming observation. $V_{ij}^{XX}, V_{ij}^{XY}, V_{ij}^{YX}, V_{ij}^{YY}$ is the visibility observed in XX, XY, YX, YY polarization respectively. $\Delta_{ij}(t)$ is the geometric delay required to phase up the visibilities from baseline between antennas i, j to the source. ν is the observation frequency. The various Stokes parameters $I^{obs}, Q^{obs}, U^{obs}, V^{obs}$ are given by

$$I^{obs} = 0.5(P^{XX} + P^{YY}) \tag{28}$$
$$Q^{obs} = 0.5(P^{XX} - P^{YY}) \tag{29}$$
$$U^{obs} = 0.5(P^{XY} + P^{YX}) \tag{30}$$
$$V^{obs} = -0.5i(P^{XY} - P^{YX}) \tag{31}$$

Thus following this procedure, we can create a dynamic spectrum of any source, and obtain $I^{obs}(\nu, t)$, $Q^{obs}(\nu, t)$, $U^{obs}(\nu, t)$ and $V^{obs}(\nu, t)$. If the source is unpolarized, which almost all astronomical sources are at the low observing frequencies relevant for OVRO-LWA, Equations 9, 10 and 11 can be modified as

$$I_{obs}(\nu, t) = M_{00}(\nu, t) I^{model}(\nu) \tag{32}$$
$$U^{obs}(\nu, t) = 2Real(p)(\nu) M_{00}(\nu, t) I^{model}(\nu) + M_{20}(\nu, t) I^{model}(\nu) \cos\delta(\nu) - M_{30}(\nu, t) I^{model}(\nu) \sin\delta(\nu) \tag{33}$$
$$V^{obs}(\nu, t) = 2Im(p)(\nu) M_{00}(\nu, t) I^{model}(\nu) + M_{20}(\nu, t) I^{model}(\nu) \sin\delta(\nu) + M_{30}(\nu, t) I^{model}(\nu) \cos\delta(\nu) \tag{34}$$

Henceforth we will keep the frequency and time dependence of various terms implicit. Combining equations 33 and 34, we obtain

$$\Phi(p) = \sum_t \left[(U^{obs} - 2Real(p) M_{00} I^{model})^2 + (V^{obs} - 2Im(p) M_{00} I^{model})^2\right] - \left[(M_{20} I^{model})^2 + (M_{30} I^{model})^2\right] = 0 \tag{35}$$

In equation 35, the summation is over all times at a single frequency. By minimizing $\Phi(p)$ we determine p for every frequency. Let us denote $\tilde{p}$ as the estimated value of p. Let us also denote $U^{obs,leak} = U^{obs} - 2Real(\tilde{p}) M_{00} I^{model}$ and $V^{obs,leak} = V^{obs} - 2Im(\tilde{p}) M_{00} I^{model}$. Then we can determine $\delta(\nu)$ by minimizing

$$\begin{aligned} \Delta_{UV}(\delta) &= \sum_t \left[U^{obs,leak} \cos\delta + V^{obs,leak} \sin\delta - M_{20} I^{model}\right]^2 + \left[-U^{obs,leak} \sin\delta + V^{obs,leak} \cos\delta - M_{30} I^{model}\right]^2 \\ &= \sum_t \left[\Delta_U(\delta) + \Delta_V(\delta)\right] \\ \Delta_U(\delta) &= \left[U^{obs,leak} \cos\delta + V^{obs,leak} \sin\delta - M_{20} I^{model}\right]^2 \\ \Delta_V(\delta) &= \left[-U^{obs,leak} \sin\delta + V^{obs,leak} \cos\delta - M_{30} I^{model}\right]^2 \end{aligned} \tag{36}$$

This also follows from equations 33 and 34. Again this procedure is done independently for each frequency. In practice, we find that it is better to use just the core antennas of the OVRO-LWA to minimize the effect of the ionosphere in the determined calibration solutions. Additionally, we also find that minimizing while Δ_V and Δ_{UV} gives the same δ for almost all frequency channels, in some cases, minimizing Δ_{UV} results in spurious solutions. Hence, now we minimize $Delta_V$.

Once the crosshand phase is determined, we can again determine $\Delta M_{10}, \Delta M_{20}$ and ΔM_{30}. However because of the reasons mentioned in Section 1.1, we determine α_Q, α_U and α_V and apply them directly to produce the final calibrated data. We again use the fact that the quiet Sun is unpolarized to determine α_Q, α_U and α_V. Mathematically,

$$\alpha_Q = \left\langle Q^{obs,corrected}/I^{obs,corrected} - Q^{beam}/I^{beam} \right\rangle \tag{37}$$
$$\alpha_U = \left\langle U^{obs,corrected}/I^{obs,corrected} - U^{beam}/I^{beam} \right\rangle \tag{38}$$
$$\alpha_V = \left\langle V^{obs,corrected}/I^{obs,corrected} - V^{beam}/I^{beam} \right\rangle \tag{39}$$

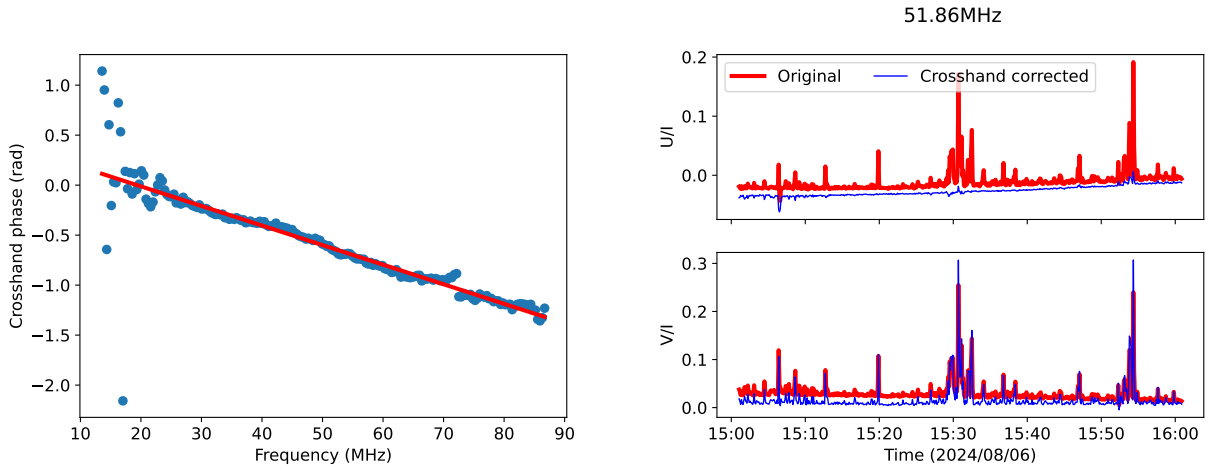

Figure 1: Left panel: The blue points shows the determined crosshand phase. Red line shows a linear fit to the determined crosshand phase. Right panel: Red line shows the fractional U^{obs} and V^{obs} in the top and bottom panels respectively. Blue line shows the fractional $U^{obs,crosshand}$ and $V^{obs,crosshand}$.

The average is taken over the quiet Sun only. Then we can use equation 26 to obtain the final calibrated solar image.

If we want to use both p and δ for calibration, ideally we should use the following equation for calibrating visibility on baseline ij.

$$V_{ij}^{obs,corrected} = R^{-1}H^{-1}V_{ij}^{obs}(H^{\dagger})^{-1}(R^{\dagger})^{-1} = FBSB^{\dagger} \tag{40}$$

$V_{ij}^{obs,corrected}$ and V_{ij}^{obs} are both 2×2 matrix. In practice, if $|p| << 1$ and $|V_{ij}^{obs,XY}/V_{ij}^{obs,XX}| << 1$, $|V_{ij}^{obs,YX}/V_{ij}^{obs,XX}| << 1$, $|V_{ij}^{obs,XY}/V_{ij}^{obs,YY}| << 1$, $|V_{ij}^{obs,YX}/V_{ij}^{obs,YY}| << 1, \forall i,j$, then the 4 elements of matrix $V_{ij}^{obs\_leak} = H^{-1}V_{ij}^{obs}(H^{\dagger})^{-1}$ in linear basis can be written as

$$V_{ij}^{XX,obs\_leak} = V_{ij}^{XX,obs} \tag{41}$$

$$V_{ij}^{YY,obs\_leak} = V_{ij}^{YY,obs} \tag{42}$$

$$V_{ij}^{XY,obs\_leak} = V_{ij}^{XY,obs} - p\left(V_{ij}^{XX,obs} + V_{ij}^{YY,obs}\right) \tag{43}$$

$$V_{ij}^{YX,obs\_leak} = V_{ij}^{YX,obs} - p^{*}\left(V_{ij}^{XX,obs} + V_{ij}^{YY,obs}\right) \tag{44}$$

2 Application of algorithm on OVRO-LWA data

2.1 Deriving polarization parameters using solar beamforming data

For this purpose, we choose beamforming data from August 6, 2024. In Section 1.1 we mentioned that the first step in doing polarization calibration is to estimate the crosshand phase. In the left panel of Figure 1 we show the estimated crosshand phase as a function of frequency. The red line shows a linear fit to the crosshand phase. It is evident that the straight line fits the crosshand phase quite well, except at the very low frequencies, where the data is anyway corrupted by large RFI and very low instrumental gains. We estimate that the delay is approximately 3 ns. In the right panel, we show the lightcurve at 51.86 MHz. The top right and top left panels show the lightcurves of U^{obs}/I^{obs} and V^{obs}/I^{obs} using red lines respectively. The blue lines show the lightcurves of $U^{obs,crosshand}/I^{obs,crosshand}$ and $V^{obs,crosshand}/I^{obs,crosshand}$ respectively. From equation 20, it is evident that U^{obs}/I^{obs} should be slowly varying with time (which in fact is just a proxy of the solar altitude-azimuth). However the large variations in U/I exactly at the location when there is strong V/I as well, which is a tell-tale signature of the incorrect crosshand phase. However, after crosshand phase calibration, $U^{obs,crosshand}/I^{obs,crosshand}$ show very small correlated variation with V, proving the accuracy of the estimated crosshand phase solutions.

Next, we determine $\alpha_Q, \alpha_U, \alpha_V$ and correct the Muller Matrix using them. Figure 2 show the normalized $\tilde{M}_{10}, \tilde{M}_{20}, \tilde{M}_{30}$ in the left panel. In the right panel, we show the final Muller Matrix terms (normalized using $\tilde{M}_{00}$) which were used to calibrate the data. While the right panel also has the effect of p, since p is constant with time, any variation in time, is necessarily due to $\Delta M_{i0}, i = 1,2,3$, which are also the errors in the model Muller Matrix. Left panel of Figure 3 shows the final calibrated data obtained using equation 26. The rows from top to bottom shows Stokes I, fractional Q, fractional U and fractional V respectively. For comparison, we have also shown the same parameters obtained by multiplying $\tilde{M}^{-1}$ to the vector $(I^{obs}, Q^{obs}, U^{obs}, V^{obs})$ in the right panel. $\tilde{M}$ is the Muller Matrix obtained from the model.

For better visualization, we show a lightcurve at 51.86 MHz at each step of the calibration procedure in top left panel of Figure 4. The red and blue lines show the result of multiplying $\tilde{M}^{-1}$ to $(I^{obs}, Q^{obs}, U^{obs}, V^{obs})$ and $(I^{obs,corrected}, Q^{obs,corrected}, U^{obs,corrected}, V^{obs,corrected})$ respectively. Black line show the final calibrated data. In the top right panel of Figure, we apply the exact same solutions on data from August 2, 2024 between 15:01–16:01 UT. In the bottom panel we apply the same solutions on data from August 6, between 23:09-00:09 UT. It is evident that after

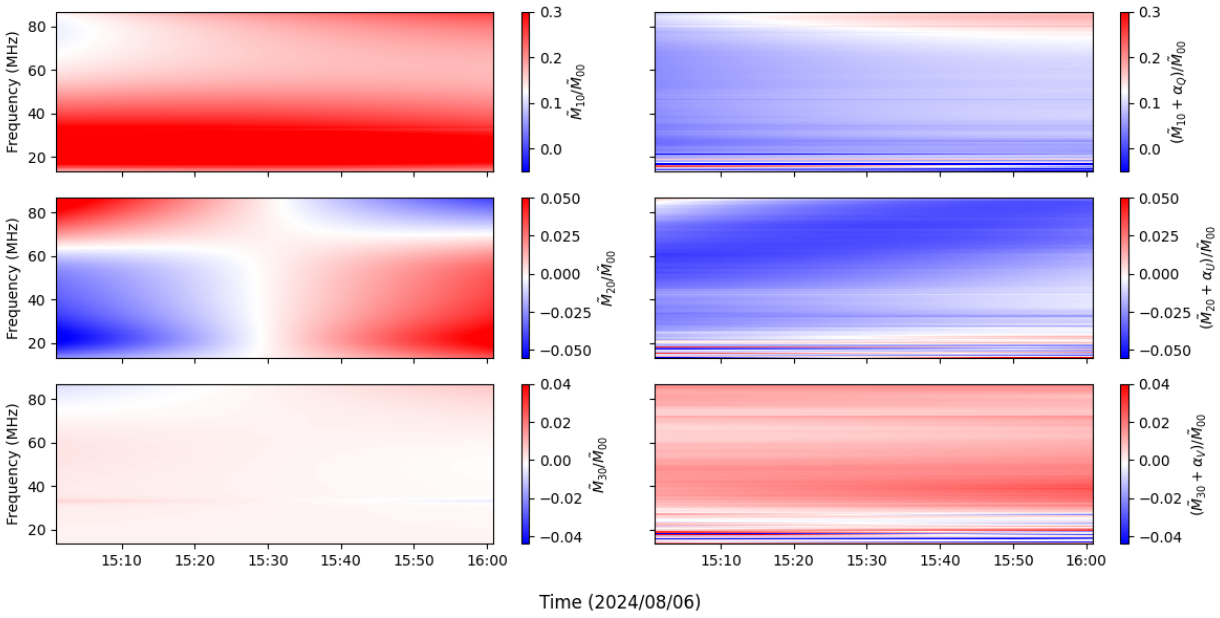

Figure 2: Left panel: Shows the spectral variation of the $\tilde{M}_{i0}/\tilde{M}_{00}, i = 1, 2, 3$ as the Sun passed through different altitude and azimuths with time. Right panel: Shows the final Muller Matrix terms (normalized using $\tilde{M}_{00}$) which were used to calibrate the data.

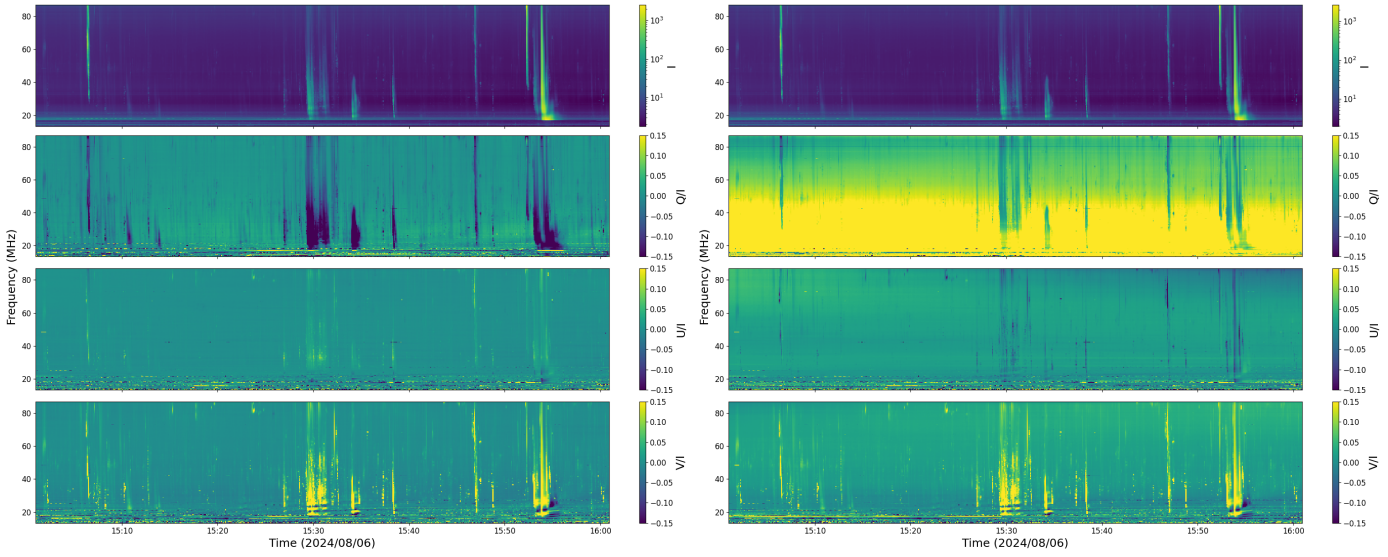

Figure 3: Left panel: Shows the final calibrated I and fractional Q, U, and V (equation 26). Right panel: Shows the result of multiplying $\tilde{M}^{-1}$ to the vector $(I^{obs}, Q^{obs}, U^{obs}, V^{obs})$.

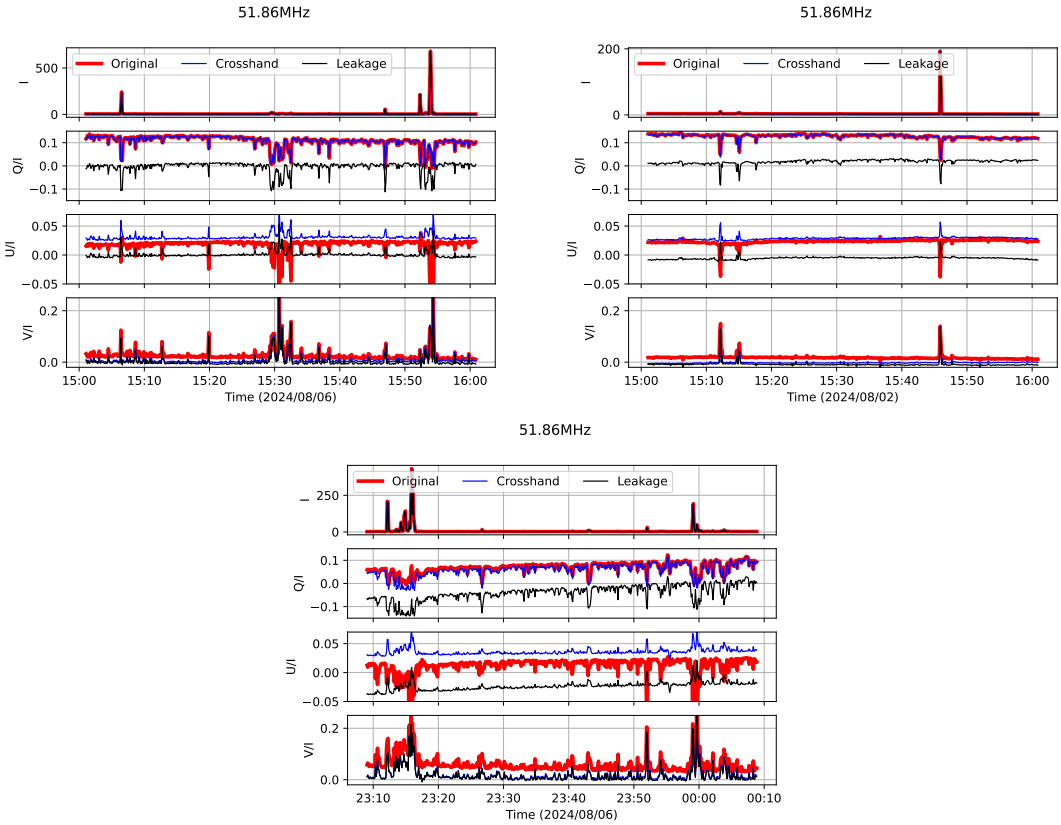

Figure 4: The red and blue lines show the fractional polarization after multiplying $\tilde{M}^{-1}$ to the vector $(I^{obs}, Q^{obs}, U^{obs}, V^{obs})$ and $(I^{obs,crosshand}, Q^{obs,crosshand}, U^{obs,crosshand}, V^{obs,crosshand})$ respectively. Black line shows the final calibrated polarization fraction. The calibration solutions are determined using data from August 6, 2024, between 15:00–16:00 UT. The same solutions have been applied for all other dates and times. Top left and top right panel shows the fractional polarizations for August 6 (15:00–16:00 UT) and August 2 (15:00–16:00 UT) respectively. Bottom panel shows the fractional polarization for August 6, 23:09 – August 7, 00:09 UT.

calibration, the quiet Sun has very low polarization in the top panels, even though the data comes from 2 different dates separated by 4 days. However, in the bottom panel, even though the solutions were derived using data, only 5 hours earlier data, the quiet Sun show residual polarization at a much larger level than that seen in the top right panel. This suggests that the solutions are dependent on the altitude-azimuth of the Sun.

2.2 Deriving polarization parameters using imaging data

We applied the method described in 1.2 on data from June 13, 2025 when Cygnus A was above an elevation of 60°[2]. There were two considerations which make these data the "ideal dataset" for this purpose.

1. Since the formalism necessarily requires good knowledge of the primary beam model, we are restricted to high elevations. The deviations from the model beam increases with decrease in elevation

2. Either of U^{beam} or V^{beam} should be detected at each timebin, for using the formalism to determine crosshand phase. However both of U^{beam} and V^{beam} increases as the elevation decreases.

Because of this opposing requirements, we need to use observations of a very strong source, whose flux density is so high that even with small M_{20}, and M_{30}, U^{beam} and V^{beam} should be detected at each time bin. Cygnus A, being the brightest source in the sky, hence is ideally suited for this purpose. Additionally, Cygnus A has a peak elevation of $\sim 87°$, which also makes determination of p easier. The limit of 60° was chosen from experience with these data. In this elevation range, while U_{beam} is detectable, $V_{beam} \approx 0$. Due to this, the π degeneracy mentioned in Section 1.1 is also present here. In principle, with improvement in the beam model, we can use observation of sources where both $U^{beam} \neq 0, V^{beam} \neq 0$, and then this degeneracy will not be there.

The determined crosshand phase (determined by minimizing ΔV in equation 36) and $2Real(p)$ and $2Imag(p)$ as a function of frequency is shown in Figure 5 and 6 respectively[3]. In Figure 7, we do a comparison between crosshand phases

[2]I think some investigation is needed on the possibility of using even lower elevation at higher frequencies. This will be helpful because with increase in frequency the flux density also decreases, which results in less polarized flux with which we can solve the crosshand phase. If we can go to lower elevations, particularly at higher frequencies, this issue can be mitigated, as lower elevation will lead to larger induced polarization, and hence larger polarized flux.

[3]There is some indication that p might also be very stable. Over the 4 datasets I have analyzed between April - August 2025, they have roughly same numbers. The stability of crosshand phase over a year is already demonstrated using solar data. I also show in the Appendix that both p and crosshand phase is definitely stable within a month.

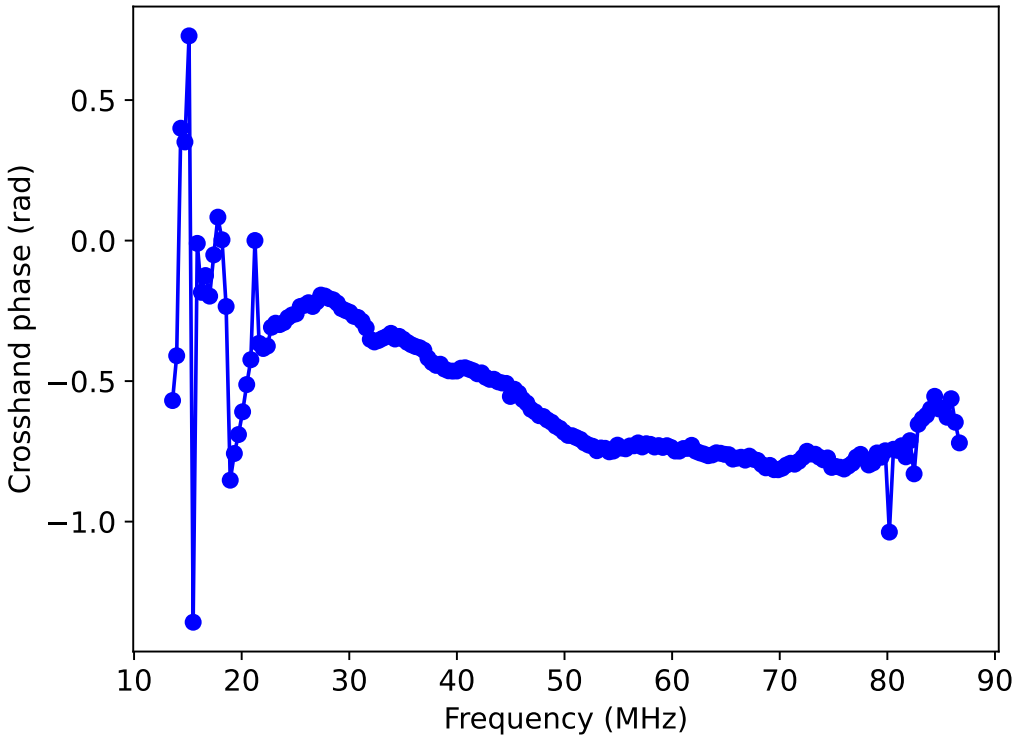

Figure 5: Shows the crosshand phase determined using Cygnus A observations from June 13, 2025.

determined by minimizing Δ_{UV} (shown with red) and Δ_V (shown in blue)[4]. It is evident that they match exactly below frequencies about 68 MHz. Then we see a clearly spurious jump in red, and after that the crosshand phases are slightly different between the two methods. This jump occurred exactly at this frequency whenever I tried to solve crosshand phase by minimizing Δ_{UV}.

In Figure 8 we show the final calibrated images in the bottom panel. For comparison, in the top panel, we have also shown the images where the only correction done is by using $\tilde{M}$. The dashed white circle shows the optical disk of of the Sun. The red contours show the degree of circular polarization at -10%, -5%, 5%, 10%. The rms and the maximum of absolute values are written in the bottom of each panel. The effect of polarization calibration is very evident in the Stokes V images. Before the calibration, there are significant Stokes V from the quiet Sun, which is not present after calibration.

We have also tested the solved parameters using astronomical sources. We apply the determined crosshand phase as well as p on the visibilities, and then image the data. The images are then corrected using $\tilde{M}$ to generate the final calibrated images. Since the determined parameters are primarily relevant for Stokes U and V, we have only shown the fractional Stokes U and V in Figure 9. For this test, we have used 10s data at a cadence of 30 minutes when either one of CygA, CasA, TauA and VirA are above 60° elevation. Each image is generated by averaging 50–55 MHz, using data across all antennas. In the bottom panel we have shown example Stokes U and Stokes V images at 06:01 and 10:00 UT. These also correspond to the times where CygA and CasA had elevation of approximately 61°. The maximum polarization fraction as well as the 5σ detection limit is indicated in top of each panel. The top row shows the original images, and bottom rows after calibration. It is clear that before calibration, Stokes V shows a lot of variation ($\sim 10\%$) across the shown elevation range. Some variation is seen in Stokes U as well, although to much smaller extent. However, after calibration, the variation in both has reduced significantly. While, both CygA and CasA is detected in both STokes U and V, the residual polarization fraction is always $\lesssim 2\%$. We discuss the reason beyond the detected polarization in Section 3.3. We also notice a curious bi-lobe structure in Stokes V. While the origin of this bi-lobe structure is fully understood yet, there are some indications that this might be due to ionospheric propagation effects. Investigations into this bi-lobe structure is provided in Section 3.4. We use data from only the core antennas, such that the resulting angular resolution is too low to see these bi-lobe structures.

3 Discussion

3.1 Database of calibration solutions

We have performed this calibration procedure at multiple days spread across the year 2024 between to produce a database of the different calibration solutions. In left panel of Figure 10, we plot the different crosshand phase solutions in the

[4]Note that we have used data from April 2, 2025 for this test

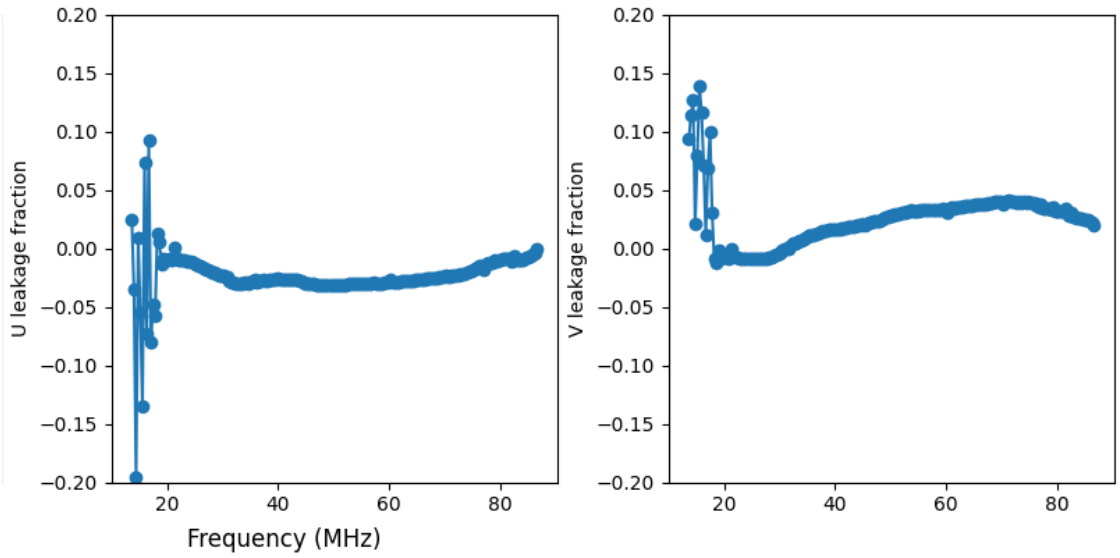

Figure 6: Results from Cygnus A observations from June 13, 2025. U leakage fraction and V leakage fraction refers to $2Real(p)$ and $2Imag(p)$ respectively.

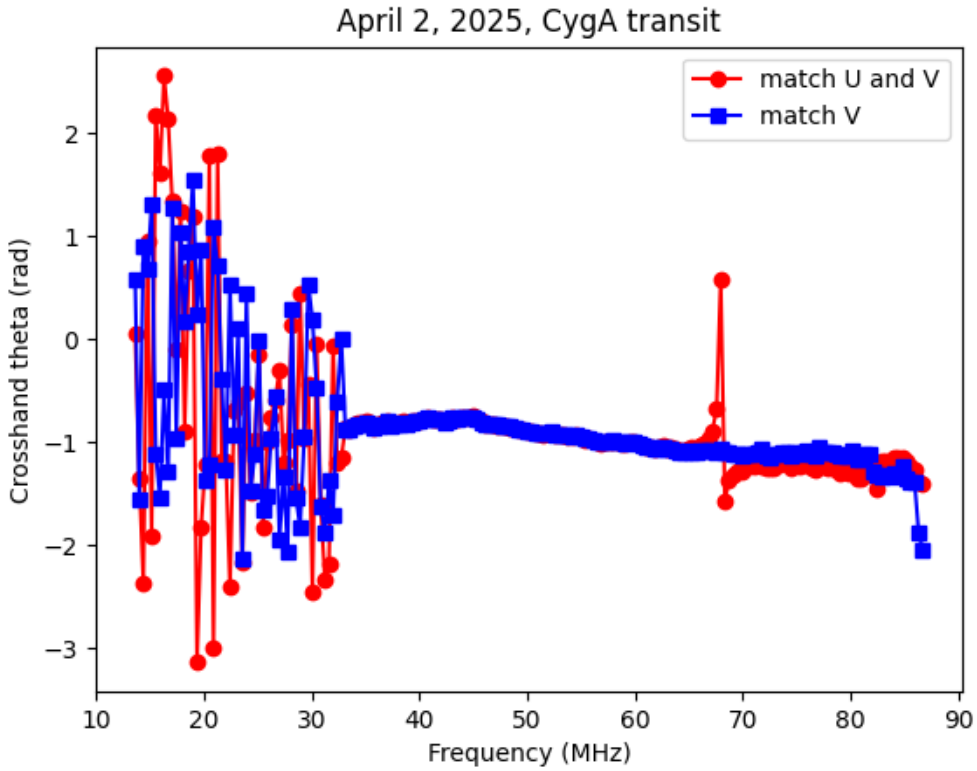

Figure 7: Shows the frequency dependence of crosshand solutions determined by minimizing Δ_{UV} (in red) and Δ_V(in red). Data from April 2, 2025 were used for this test.

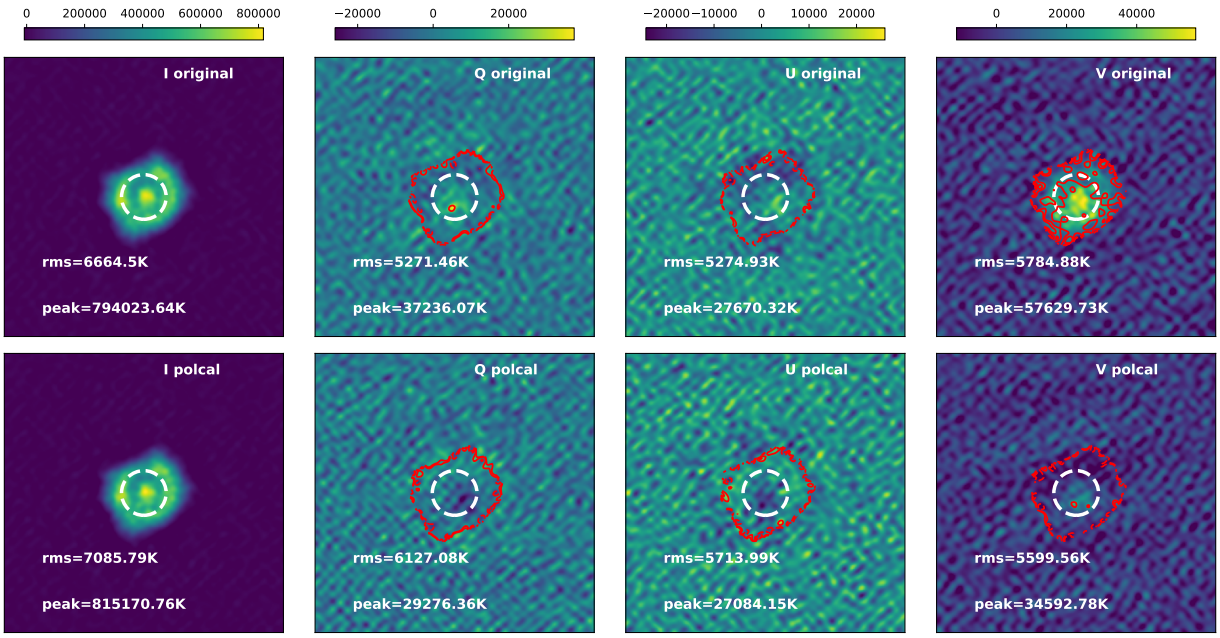

Figure 8: Shows the result of polarization calibration where all solutions were obtained using method described in Section 1.2. The crosshand phase solutions were determined using CygA observation. αs were determined using the quiet Sun regions in these images. Top panel: Shows the result of multiplying $\tilde{M}^{-1}$ to $(I^{obs}, Q^{obs}, U^{obs}, V^{obs})$ images. Bottom panel: Shows the final calibrated images (equation 26). The contours shows the fractional polarization of -10%, -5%, 5% and 10%. The rms and the maximum absolute value of each image is also indicated at the bottom pf each panel. The white dashed circle show the optical disk of the Sun.

database. Each color represents an independent dataset. Our tests suggested that the crosshand phase is very stable, in some case, even across months. Hence each dataset is separated by about a month. In the right panel of Figure 10 we show a histogram of the difference of the phase solutions, between frequencies 30–88 MHz. We do not consider lower frequencies as the data are quite often affected by a lot of RFI. We find that the solutions are very similar, even when separated across months. In Figure 11 we provide further evidence of this stability. We apply crosshand phase solutions from December 9, 2024 on data from November 11, 2024. In the top left panel, we have shown $U^{obs,corrected}/I^{obs,corrected}$ and $V^{obs,corrected}/I^{obs,corrected}$. In the top right panel, we have shown U^{obs}/I^{obs} and V^{obs}/I^{obs}. For better visualization, in the bottom panel, we have shown the fractional U and V lightcurve at 51.86 MHz. It is evident that the crosshand solutions obtained from December 9, have reduced the fractional U significantly even on November 11. And this is visible, not only during the radio bursts. We also find that before the crosshand phase calibration, the fractional U and V were highly correlated in the times when bursts are absent, for example between 19:00 –19:40. However, after crosshand phase calibration, $V^{obs,corrected}/I^{obs,corrected} \approx 0$ during these times, although $U^{obs,corrected}/I^{obs,corrected}$ still has a negative slope similar to that observed in U^{obs}/I^{obs}.

In Figure 12 we have shown the variation of $\alpha_Q, \alpha_U, \alpha_V$ with zenith angle and azimuth. The zenith angle increases radially. The tracks are obtained as the Sun moves across the sky and we generate the solutions using solar data across a day. Thus longer tracks indicate that it is taken from a local summer time. The fact that the variation is quite smooth, even though, the data spans a large fraction of a year, suggests that p is quite stable, and is much smaller than ΔM_{10}, ΔM_{20} and ΔM_{30}, particularly at low elevations. We find, particularly when the Sun starts from low elevation and moves to quite high elevation, ΔM_{10}, shows the highest variation. The value is lowest when the Sun is at the smallest zenith angle. This implies that the variation of $\Delta M_{i0}, i = 1, 2, 3$ is a function of altitude-azimuth and not the local temperature.

3.2 Appropriate choice of datasets for calibration

As discussed in Section 1.1 we use the fact that the quiet sun is unpolarized for determining the calibration solutions. However, it must be noted that even though the quiet Sun is unpolarized, due to the fact that M is not a diagnoal matrix, there will be induced polarization. This makes $(I^{beam}, Q^{beam}, U^{beam}, V^{beam})$ a polarized source. This is very important for crosshand phase determination. In fact, if $(I^{beam}, Q^{beam}, U^{beam}, V^{beam})$ is unpolarized, then we cannot solve for the crosshand phase in general (Sault et al., 1996). However the method outlined in 1.1 puts additional constraints. From equation 14 it is clear that if for some dataset U^{obs} and V^{obs} is approximately constant, then the equation becomes degenerate for δ. This implies that for achieving proper crosshand phase calibration, we need variable U^{obs} and V^{obs}. Higher variability leads to more accurate crosshand phase estimation. This variability can come either from beam induced polarization, or polarized radio bursts. However, care should be taken to ensure that the circular polarization is low enough that $M_{23}V^{model} << M_{20}/M_{00}I^{obs}$. This comes from the fact that we have ignored $M_{23}V^{model}$ in equation 14. We also note here that while Dey et al. (2025) demonstrated that linear polarization can be observed from the Sun, the sources of linear polarization are quite compact. This implies that apart from very strong bursts where the coherent emission

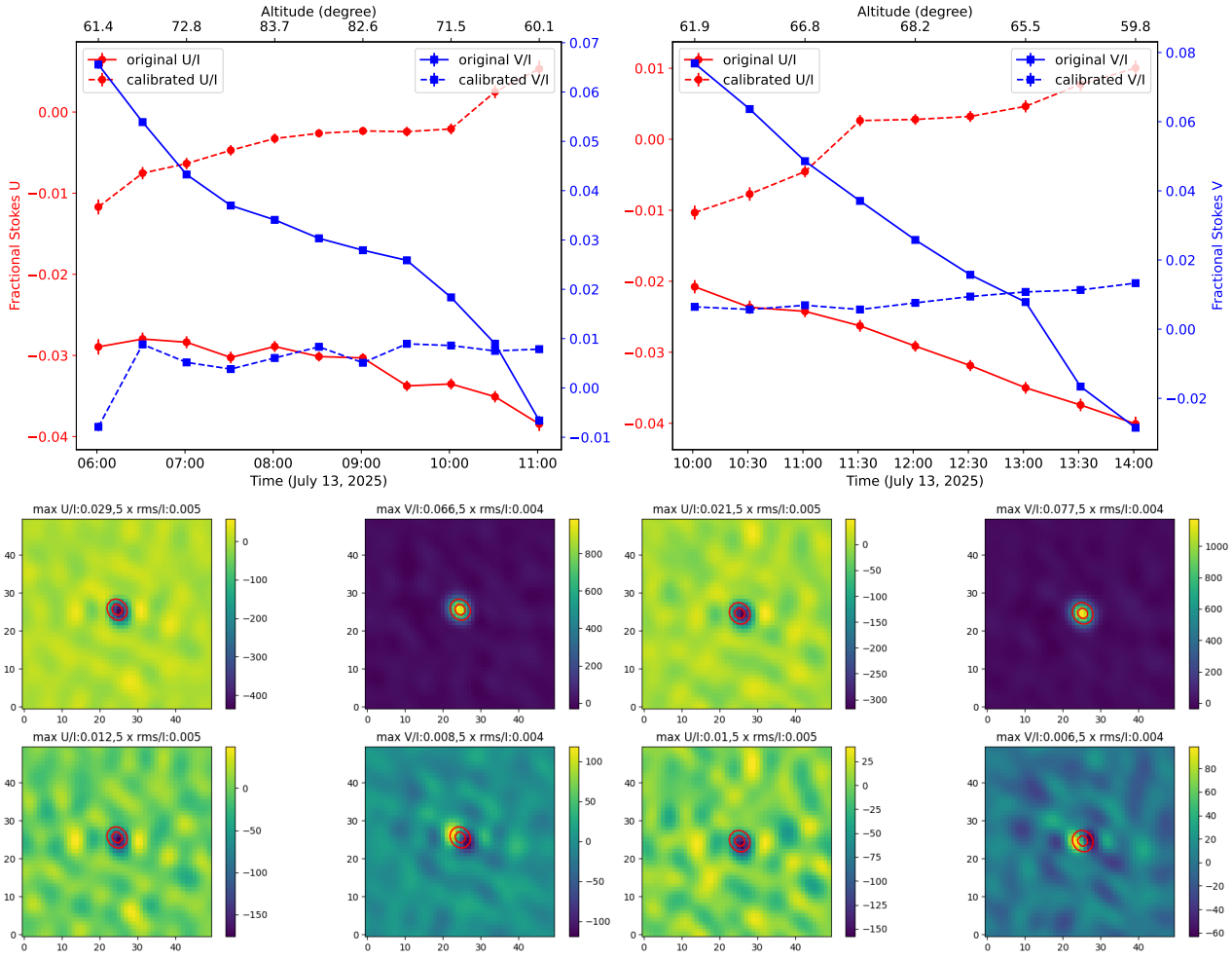

Figure 9: Top panel: Shows the fractional Stokes U and V after multiplying $\tilde{M}^{-1}$ to $I^{obs}, Q^{obs}, U^{obs}, V^{obs}$ using solid red and blue lines respectively. The fractional $U^{calibrated}/I^{calibrated}, V^{calibrated}/I^{calibrated}$ are shown using dashed red and blue lines respectively. The fractional U and V are shown on the left and right Y-axis respectively. The top left and top right panels shows the time periods when CygA and CasA are above 60 degrees elevation. All solutions were determined using the time period when CygA was above 60 degree elevation and were applied to all other times. Since CygA and CasA are unpolarized at these frequencies, any deviation from zero indicates residual polarization. Bottom left panel: Shows example Stokes U and Stokes V image at 06:01 UT. The top left and right panels show Stokes U and V, after multiplying $\tilde{M}^{-1}$ to $I^{obs}, Q^{obs}, U^{obs}, V^{obs}$, centered at CygA. The residual polarization fraction and $5\sigma/I^{max}$ is also indicated on top of each panel. I^{max} is the peak intensity of the image. If the residual polarization fraction is greater than the $5\sigma/I^{max}$, that implies that spurious polarization is detected. The bottom left and right panels show $U^{calibrated}, V^{calibrated}$ respectively. The bottom right panel shows the image at 10:00 UT, centered at CasA, in the same format as the bottom left panel.

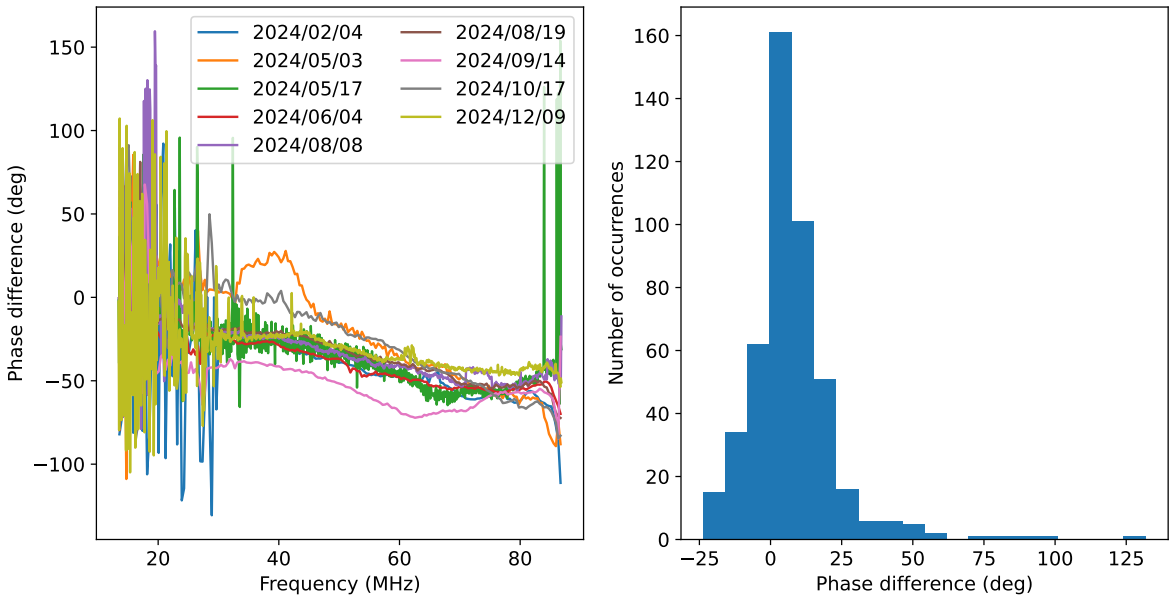

Figure 10: Left panel: Shows the crosshand phase solutions present in the database we have created using data spanning from February – December 2024. Right panel: Shows the histogram of the difference of crosshand phase determined at each frequency on different dates. For the histogram, we have only considered solutions for frequencies between 30–88 MHz.

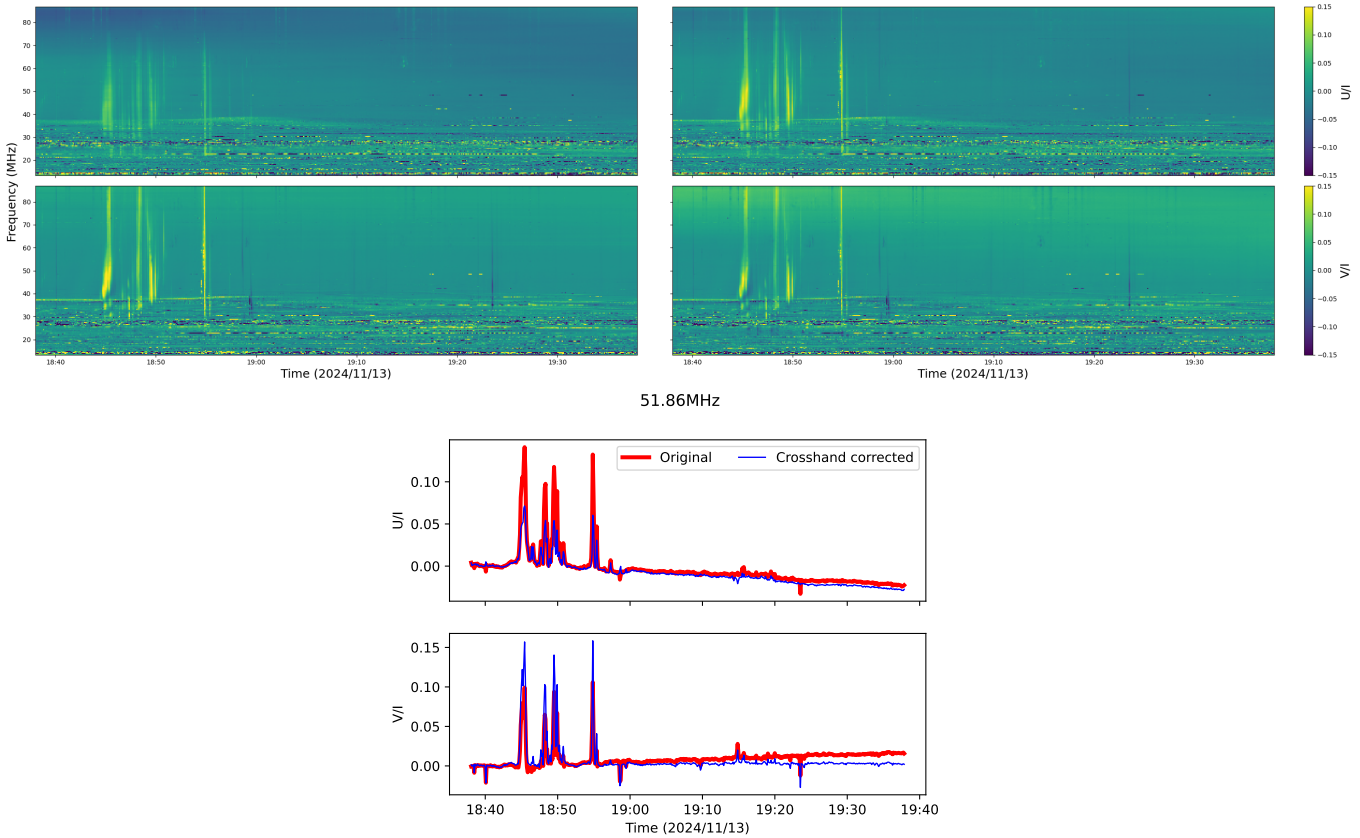

Figure 11: Top left panel: Shows the fractional $U^{obs,corrected}, V^{obs,corrected}$. Top right panel: Shows the fractional U^{obs}, V^{obs}. Bottom panel: Red and blue lines show the observed Stokes data and after crosshand phase correction respectively.

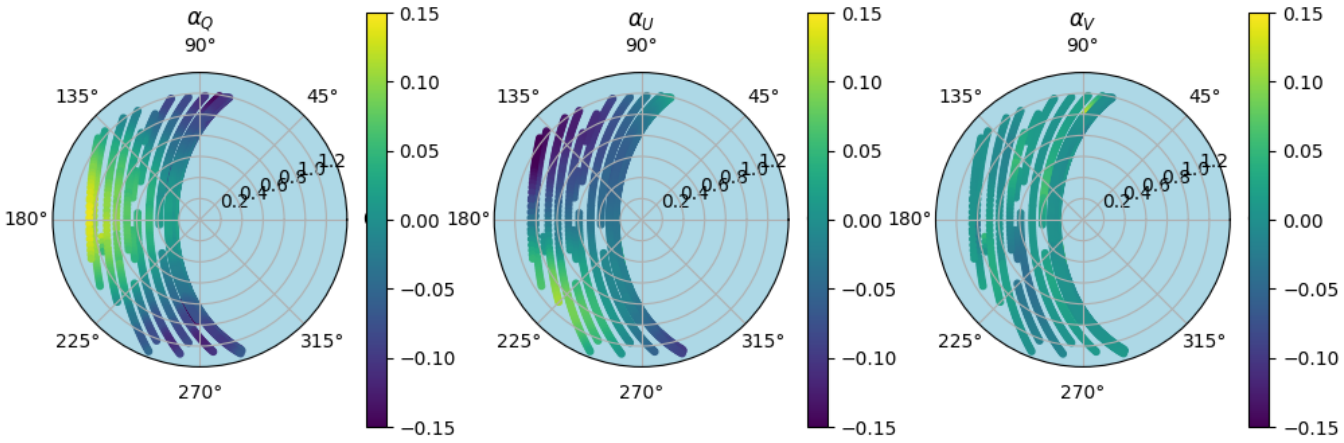

Figure 12: The left, middle and right panels show $\alpha_Q, \alpha_U, \alpha_V$ as a function of zenith angle and azimuth. These solutions are available in the database we have created using a small sample of data from 2024.

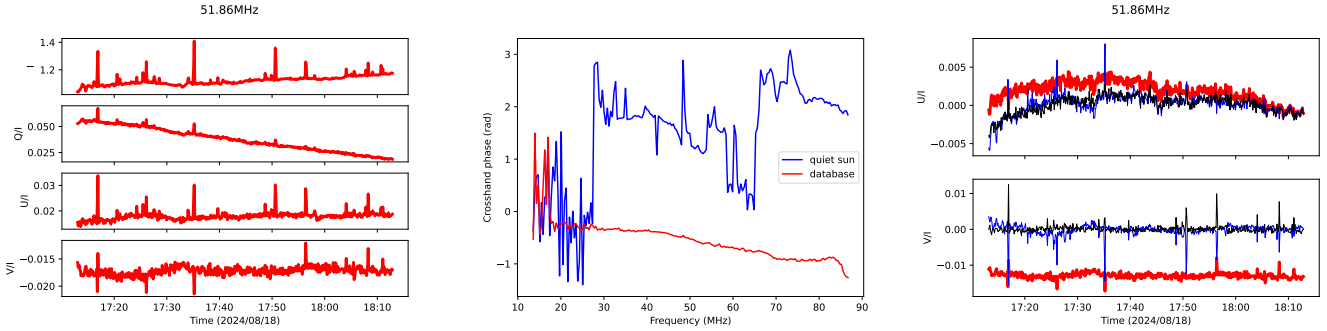

Figure 13: Left panel: Shows the time evolution of $I^{obs}, Q^{obs}/I^{obs}, U^{obs}/I^{obs}, V^{obs}/I^{obs}$ at 51.86 MHz. Middle panel: Blue line shows the crosshand phase estimated for each frequency channel using the formalism described in Section 1.1 on these data. Red line shows the crosshand phase solutions from our database. Right panel: Shows the time evolution of $U^{calibrated}/I^{calibrated}, V^{calibrated}/I^{calibrated}$. Blue line shows the case where the crosshand phase solutions are the ones shown in blue in middle panel. Red line shows the case where the crosshand phase solutions are the ones shown in red in middle panel. In both cases, the leakage solutions are independently determined following method described in Section 1.1. Red line shows the effect of multiplying $\tilde{M}^{-1}$ to $I^{obs}, Q^{obs}, U^{obs}, V^{obs}$.

dominates the total flux density of the Sun, the linearly polarized flux will be a tiny fraction of total flux density of the Sun and hence can be safely ignored. Additionally, in all the datasets we have chosen for crosshand phase estimation, the dynamic spectrum was dominated by quiet Sun, with only a few Type III radio bursts (similar to that seen in Figure 4). This ensured that the total Stokes U flux in the DS is dominated by the leakage of Stokes I into U from the quiet Sun. Due to this property of the carefully chosen datasets which were used for crosshand phase calibration, we do not expect that the assumption that Stokes U is 0 leads to significant errors in the determined calibration solutions. In Figure 13 we show the effect of determining crosshand phase from a data where the V^{beam}, U^{beam} have very little variability. The left panel shows the time profile of $I^{obs}, Q^{obs}/I^{obs}, U^{obs}/I^{obs}, V^{obs}/I^{obs}$. It is clear that both V^{obs}/I^{obs} and U^{obs}/I^{obs} is practically constant, with minor variations at the level of $\approx 1\%$. Additionally, these variations do not seem to correlate between U and V. In the middle panel, we have shown in blue the crosshand phase determined from these data. The red line shows the crosshand phase from the nearest day available in the database. The crosshand phase obtained using the quiet sun data has almost no similarity with the expectation that in absence of apriori correction, the crosshand phase should be primarily follow a linear relationship with frequency. However, for better verification we produce two datasets correcting using these two crosshand phase solutions. Next we follow the exact same procedure for determining $\Delta M_{i0}, i = 1, 2, 3$ and then determine the final calibrated data. In the right panel, we have shown the final calibrated data. The blue and black lines show the case where we used crosshand phase determined from the quiet sun data and that determined from the database respectively. For comparison, we have also shown the result of multiplying $\tilde{M}^{-1}$ to the observed data without doing any other correction, using red. We find that the blue curve shows large fractional U even in cases, when no such peak exist in the red one. However, no such high fractional U is seen in the black curve.

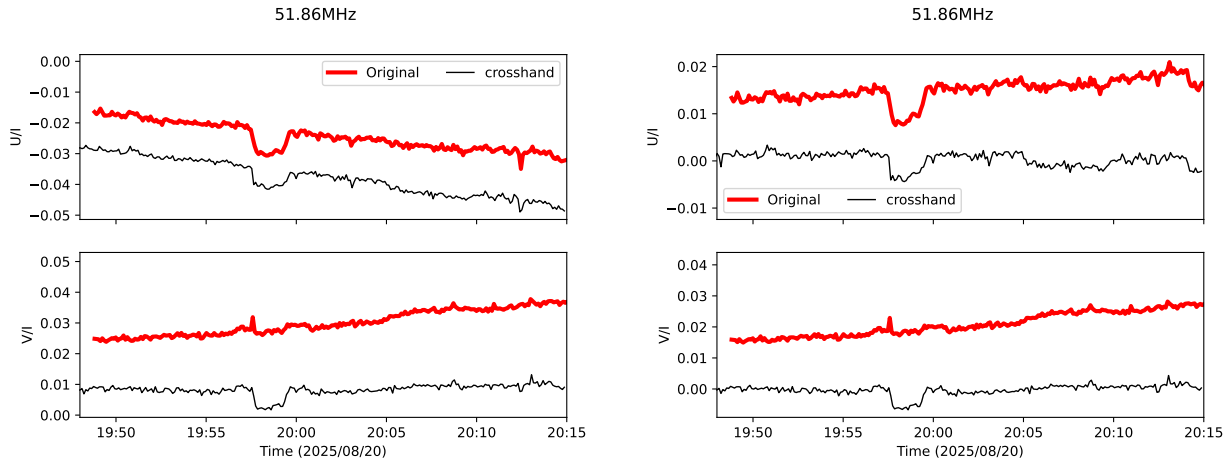

Figure 14: Shows the effect of applying crosshand phase solutions determined using CygA observations on solar data. Black line shows the data where the crosshand solutions were applied before the data are recorded. Red line shows the data when no crosshand phase correction is applied. Top and bottom panels show the fractional U and V respectively. Left panel: Shows the lightcurve of fractional U^{obs}, V^{obs} at 51.86 MHz. Right panel: We determined α_U, α_V corresponding to the altitude-azimuth of the Sun and applied on both these datasets. Red line again shows the effect of this correction, where the data have not gone through any crosshand phase correction. Black line shows the effect of this correction where the crosshand phase, determined from CygA observations, were applied before recording the data.

3.3 Inter-usability of parameters obtained from beamforming and imaging data

Here we have discussed two different ways of determining polarization parameters from the two different kinds of data products available from OVRO-LWA. Although the parameters play same role in the both the data products, they may not be the right relevant parameters which need to be corrected. The crosshand phase is property of the reference antenna, which is used during the bandpass calibration step. In some cases, a specific reference antenna may not be used in bandpass calibration step, instead of which the array-averaged phase is set to zero. Strictly speaking, the crosshand phase is the phase difference between the reference phases used for the X and Y polarizations. Hence, as long as the same phase reference is used for calibrating the image data, and the calibrations applied on the beamforming data, the crosshand phase derived from imaging data can be applied on the beamforming data as well. Apart from the crosshand phase, we have also solved for the $\alpha_Q, \alpha_U, \alpha_V$. From equations 20 and 24, it is clear that α_U, α_V is a linear combination of primary beam errors $(\Delta M_{i0}, i = 2, 3)$ and also errors due to the signal chain (p). p, in reality, is an antenna dependent quantity, which we have ignored in this formalism. The p, we have used here, is some sort of array-averaged quantity, which we have used to decrease the complexity of the calibration procedure. However, since the antennas which are used for beamforming may be different from the antennas used for imaging, the exact value of the array-averaged quantity can be different. Hence α_U, α_V determined from beamforming data may not be applicable for imaging data, and vice versa. Based on this logic, we can also conclude even α_U, α_V determined from two different beamforming data, which have been observed using two different sets of antennas, may not be same. Additionally, α_U, α_V are primarily dominated by errors in the primary beam model. While, in this work, we assume that the primary beam of each antenna is identical, in reality, the mutual coupling between dipoles will lead to deviations from this assumption. The deviation will depend on the distribution of neighbouring antennas, and will ultimately make OVRO-LWA a heterogeneous array. Generation and usage of primary beam models including the mutual coupling is still under investigation and is outside the scope of this work.

In Figure 14 we show a demonstration of this. We applied the crosshand phase solutions determined using astronomical sources during the recording of the beamforming data. No separate crosshand phase calibration was applied. For comaprison, we also took some test data simultaneously, where we did not apply the crosshand phase solutions. In the left panel of Figure 14 we show the fractional U and V from these two datasets. Black line shows the standard data stream where the crosshand phase has been applied during recording. Red line shows the test data taken for comparison. During the time of this observation, the elevation of the Sun was about 60°. Additionally the Sun was very quiet, apart from a Type III radio burst. We find that the fractional U and fractional V both show a linear trend and apart from about a 2 minute window between 19:58–20:00, are highly correlated for the test dataset. It is interesting to note that this exception is exactly the time of the Type III radio burst. As mentioned in Section 1.1 the quiet Sun is unpolarized. Hence any correlation seen in fractional U and fractional V is due to the crosshand phase. Hence it is understandable that the test data, where no crosshand phase solution has been applied, shows such high correlation. No such high correlation is seen in the regular data. Additionally, the regular data shows very little fractional V as well, in contrast to the test dataset. Due to the exceptional stability of the system, any deviation from a constant fractional U and V are definitely due to errors in the beam model. We have already discussed in Section 3.1 that we have created a database only using data from the year 2024. We corrected for the α_U, α_V using the database, and show the final calibrated data in the right panel of the same figure. It is clear that in the quiet Sun regions, both the fractional U and V have gone to 0. This shows that indeed, we can use the crosshand phase solutions from imaging data of astronomical sources, along with αs

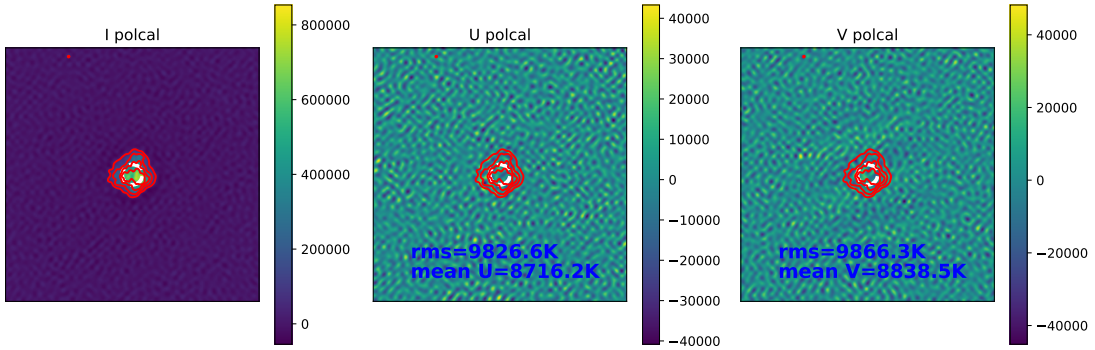

Figure 15: Shows the final calibrated solar image, generated by integrating 10s and 50–55 MHz band at 20:10:05 on August 20, 2025. The crosshand phase solutions are same as that shown in blue in middle panel of Figure 14. αs were also determined from the database. The average U and V determined from the quiet Sun region is indicated at the bottom. The rms of Stokes U and Stokes V images are also indicated.

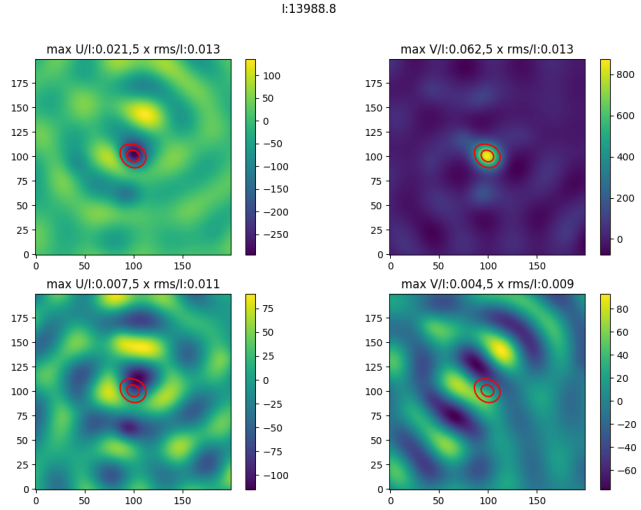

Figure 16: Shows images in the same format at bottom left panel of Figure 9. The time and frequency band of the image is also same. The only different is that, in contrast to the earlier image, here we have used only antennas which are located in the core of the OVRO-LWA. These antennas are the ones, data from which were used to determine p, crosshand phase.

from beamforming data to calibrate the solar beamforming data.

Next, we do another experiment where we use imaging data from August 20, 2025, at 20:10:05. For consistency, we use data between 50–55 MHz, which covers the frequency which is shown in Figure 14. We apply the crosshand phase solutions from astronomical source observations. The αs, however, were taken from the leakage database. We again note that here that the leakage database only uses data from 2024. The resulting image in Stokes I, U and V is shown in Figure 15. It is evident that, as expected from Figure 14, we do not detect any Stokes U and Stokes V after calibration. We can use these images to calculate an upper limit for the residual leakage fraction in U and V. Using the mean Stokes I intensity of the quiet Sun, and a detection threshold of 3σ, where σ is the rms, the upper limit on the residual polarization fraction in U and V is about 11%. This upper limit is quite high, and if the residual leakage fraction is so high, would lead to high Stokes U and Stokes V flux during times of radio bursts. However individual radio bursts are not very good for calibration purposes, as their polarization properties are unknown. Hence we turn to data from astronomical sources to gain more understanding on the inter-usability of solutions.

In Section 2.2 we determined p and crosshand phase using astronomical sources. We mentioned that we use data from the core antennas to determine these parameters. In Section 2.2, we also applied the determined parameters on data from all baselines, and showed that although the parameters reduce the observed polarization significantly, there is a non-zero residual polarization. However, as shown in Figure 16, if we image only using the core antennas, the residual polarization fraction becomes undetected. Additionally, the 3σ upper limit on the residual Stokes U and Stokes V is $\sim 0.5\%$. This demonstrates that the when the same antennas are used for beamforming and imaging, then the calibration solutions can be interchangibly used.

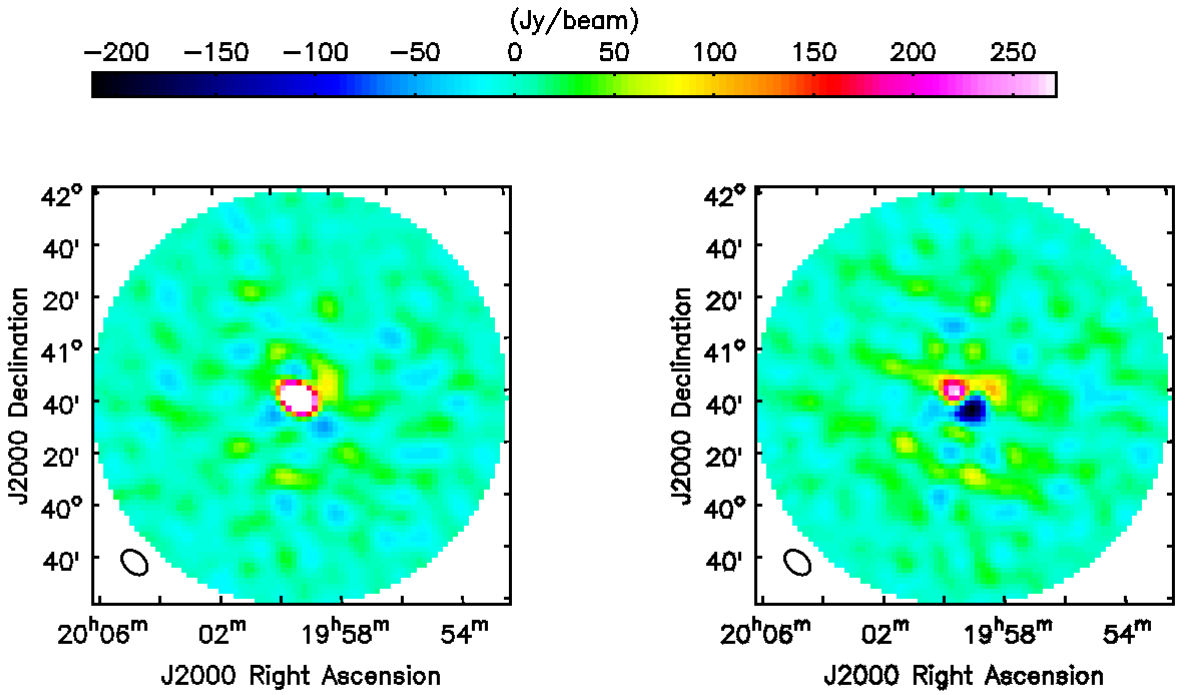

Figure 17: Shows Stokes V images at 19:30:06 UT on January 28, 2025 at 59–64 MHz band. Left panel: Only bandpass solutions were applied. Right panel: Both p and crosshand phase have been applied. The colorbar is such that it scales from maximum to minimum corresponding to the calibrated image shown in the right panel. This resulted in the left panel being highly saturated, as the maximum was $\approx 811 Jy/beam$. The minimum was only $-54 Jy/beam$.

3.4 Why do we observe the bi-lobe structures in Stokes V?

Since, this was a surprising observation, we tried to understand the reason of this by characterizing this bi-lobe structure. Below we list each of the tests and characterization done.

3.4.1 Is this an error in determining correct p?

Since correcting for p is equivalent to subtracting a constant fraction of Stokes I image, the bilobe cannot be created by erroneous p.

3.4.2 Is this an error of determining the crosshand phase?

We first note that crosshand phase conserves the $(U^{obs})^2 + (V^{obs})^2$. Hence if, the bilobe is observed in V^{obs}, then it cannot be mitigated using crosshand phase. This is also true, if the bi-lobe is seen in $V^{calibrated}$. Since crosshand phase conserved $(U^{calibrated})^2 + (V^{calibrated})^2$, an errorneaous crosshand phase can never create a bi-lobe. We have verified this using data at 59 MHz from January 28, 2025 at 19:30:06 UT. In Figure 17 we show in the left and right panels CygA Stokes V images before and after polarization calibration respectively. The colorbar is such that it scales from maximum to minimum corresponding to the calibrated image shown in the right panel. This resulted in the left panel being highly saturated, as the maximum was $\approx 811 Jy/beam$. The minimum was only $-54 Jy/beam$.

Since we have also mentioned in Section 3.4.1, we first correct the dataset using the determine p and produce images at a grid of trial crosshand phases in $[0, \pi]$ in steps of 2°. For each image, we determine the maximum and minimum value of Stokes V for image produced from each trial crosshand phase. Same was done for Stokes U as well. In Figure 18, we show the result of this experiment. Bilobe structure will be observed if $max(V) \sim -min(V)$. Similar relation also is valid for Stokes U. We find that there is no crosshand phase for which $max(V)/min(V) >> 1$ or $max(V)/min(V) << 1$. This implies the bi-lobe structure is present at all trial crosshand phases. We also note that the angles at which Stokes V lobes are weak (at minimum, the lobe strength is about 0.2% of I), are the exact angles where Stokes U lobes are the strongest. This is expected because of the conservation of the vector norm in the UV space.

3.4.3 Characterizing the bilobe structure and strengths

For this test, we determined p and crosshand phase using data from January 28, 2025. The solutions were applied between January 20– Feb 14. We have imaged one 10s data analyzed per calibrator per day. For January 28, all times when at least one A-team source was above 60 degree elevation was imaged.

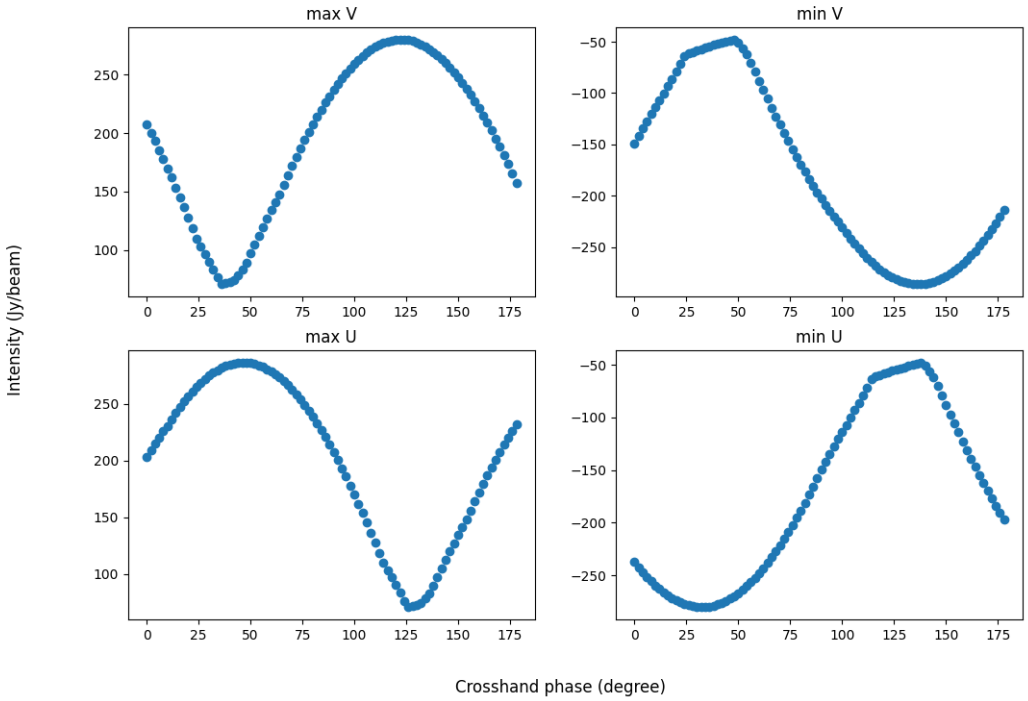

Figure 18: Show the maximum and minimum values of Stokes U and V at the source location. The images were generated by applying trial crosshand phases on a dataset corrected for bandpass and p.

1. The orientation of the bi-lobe seems to be time-dependent. In Figure 19, we show how the orientation of the CygA Stokes V bilobes are changing with time. We have used 41–46 MHz band from January 28, 2025.

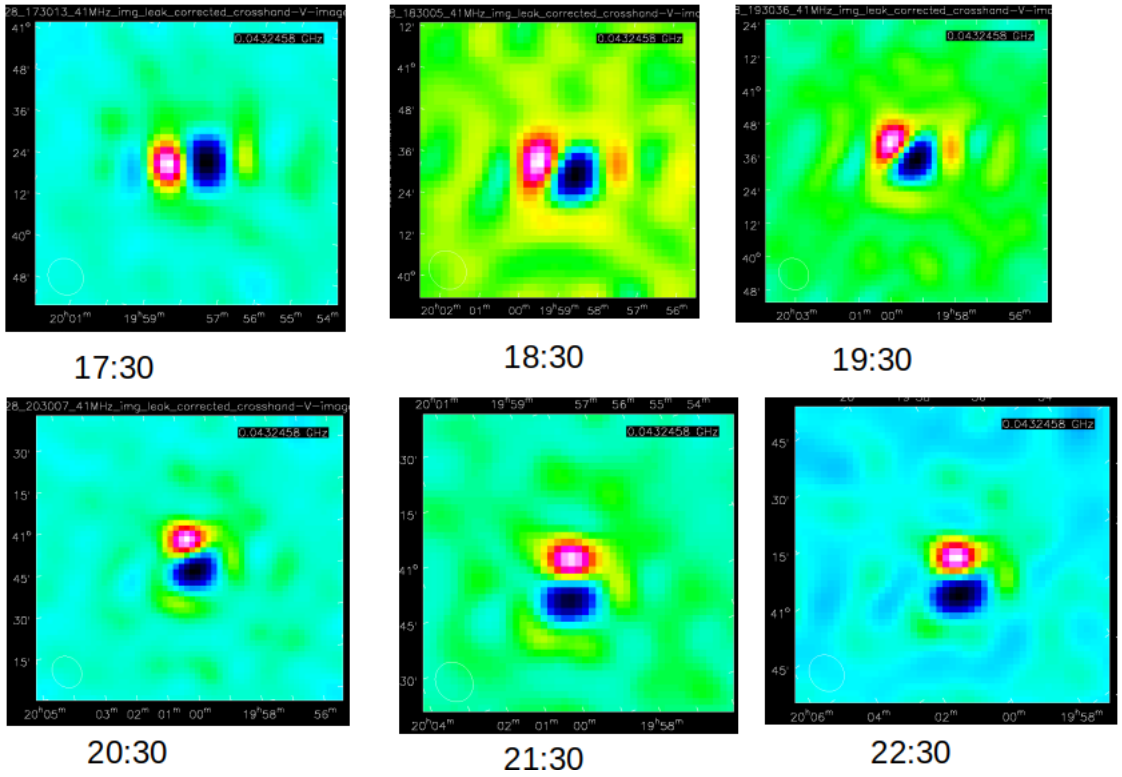

Figure 19: Shows the variation of bilobe orientation at 41–46 MHz with time. Data are taken from January 28, 2025. The source shown in CygA, after calibration. Calibration factors are exactly same.

2. The bilobe orientation is not always same for all sources. We have observed multiple instances, where it was same for all sources as well. In Figure 20 we show CasA and CygA at 18:57:46 of February 2, 2025 at 55 MHz. The time is very close to CygA transit. During this time, we see bilobe in Stokes V in both the sources. However the orientation of the bilobe is very different between the 2 sources. In fact, in some instances, we find that bi-lobe is

detected in some sources, and remains undetected in others. In Figure 21 we show images from 19:26:11 of January 26, 2025 at 73–78 MHz band. Left and panel shows CygA and CasA respectively. Additionally, it is worth noting that the CygA was close to zenith during this time. We find that the Stokes V bilobe is detected in CasA, but remains undetected in CygA at the same time instant. The same behaviour was seen in Same behaviour in 69, 64, 59, 55 MHz bands as well. Note that 78 and 82 MHz data were unavailable for these days. It is also worth noting that Stokes bilobe was again not seen during CasA transit on same day at 22:50:18 UT. On January 27, we see the bilobe on both sources at 19:19:14. Additionally, the lobe orientation was same for both CygA and CasA.

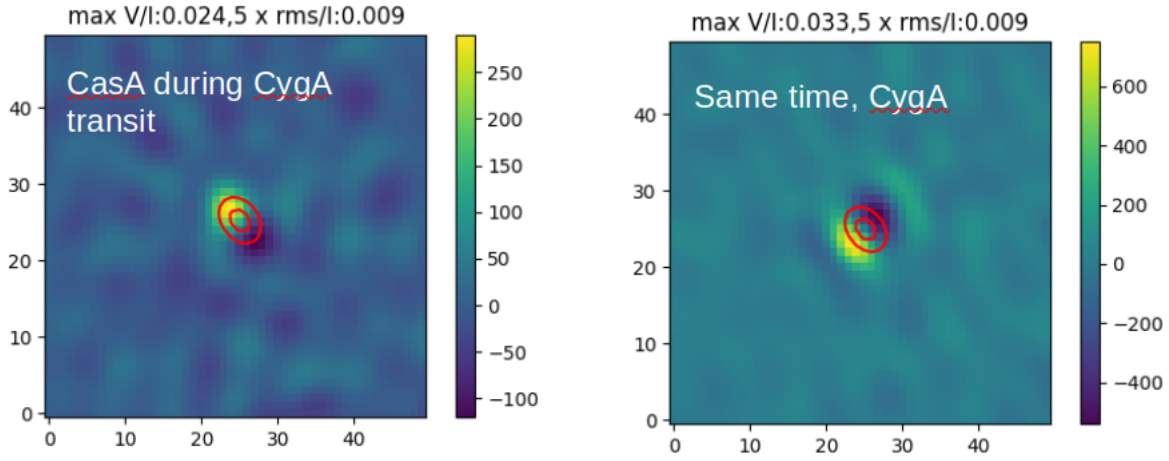

Figure 20: Left and right panels show CasA and CygA images at 18:57:46 of February 2, 2025 at 55–59 MHz band respectively.

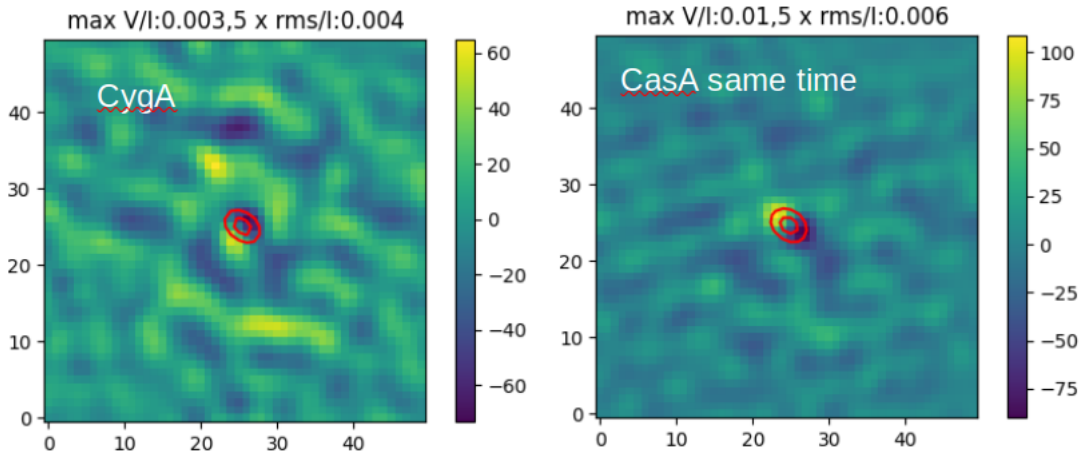

Figure 21: Left and right panels show CygA and CasA images at 19:26:11 of January 26, 2025 at 73–78 MHz band respectively. This time was close to CygA transit.

3. We find that the separation between bilobe decreases with increase in frequency. In Figure 22 we show CygA Stokes V images at 19:30:06 from January 28, 2025 at multiple frequencies. During this time, CygA had elevation of approximately 86°. In Figure 3 we fit the bilobe separation as a function of $1/\nu, 1/\nu^2, 1/\nu^3$. The errorbars correspond to 1 pixel. The data can be fairly well fit by all 3 functions.

4. We have also investigated if there is any difference between bilobes at day and night. In Figure 23 we have shown a histogram of bilobe separation by combining images at bands between 36–73 MHz. 32MHz images were not generated for all A-team sources[5] Data were taken from 28 January, 2025. The bilobe separation was calculated in the following manner:

   - Choose the maximum and minimum pixels in Stokes V image, located within 2 PSFs of the peak in Stokes I.
   - If the maximum or minimum is detected with SNR 3, and the other peak is detected with a SNR of at least 1.5, then the separation is computed as a fraction of the PSF major axis.
   - Else, the separation is set to 0.
   - CasA and CygA are always attributed to daytime. VirA and TauA are attributed to night time.

   It is evident that during night, there is a large number of images where the bilobe is not detected. However, bilobe is almost always detected during day.

[5] I cannot remember what was the reason behind this, at a time when I am writing this note.

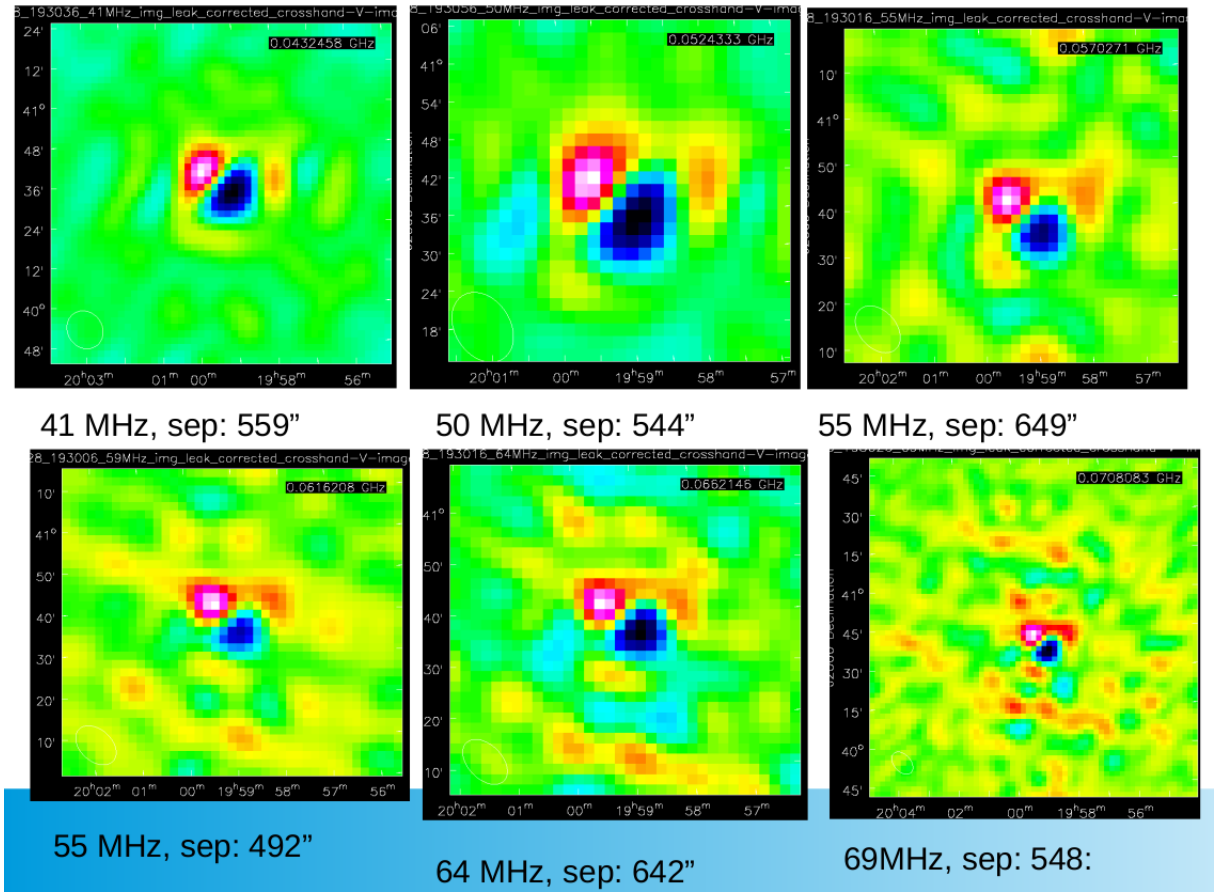

Figure 22: CygA Stokes V images at 19:30:06 from January 28, 2025 at multiple frequencies. The bilobe separation in arcseconds and the frequency of each image is mentioned at bottom of each panel.

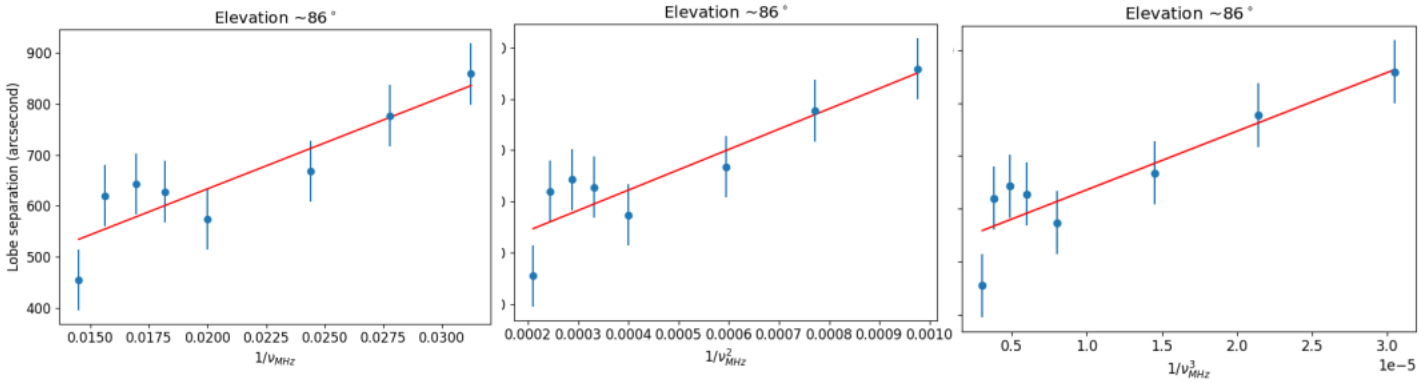

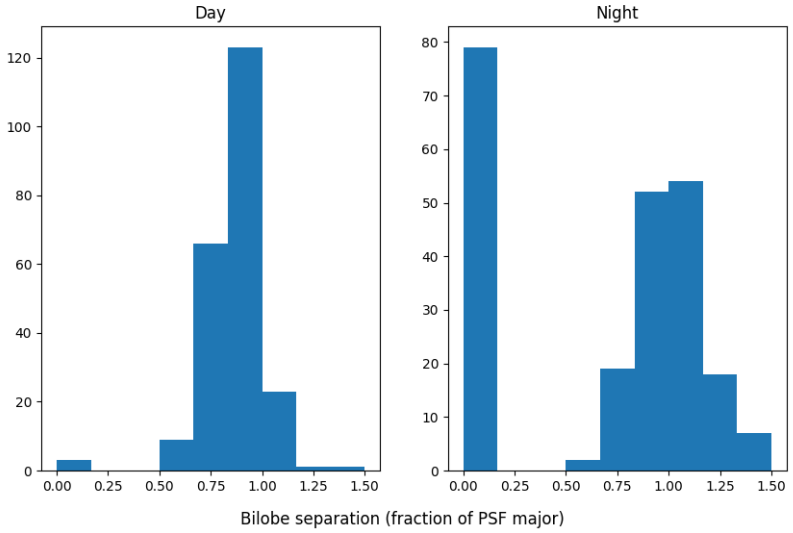

Figure 23: Histogram of Stokes V bilobe separation as a function of day and night.

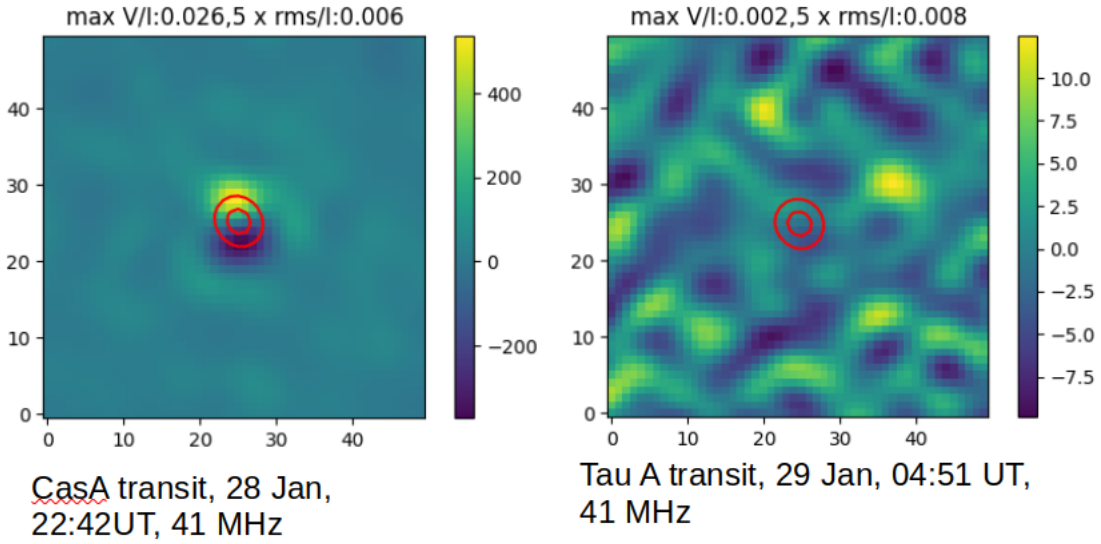

Figure 24: Left panel: CasA transit at 22:42 UT on Jan 28, 2025. Image is at 41 MHz. The bilobe structure is clear. Right panel: TauA transit a few hours later. Image is again at 41 MHz. Bilobe is not detected.

5. Since TauA and VirA were present at night, and they are weaker sources, we investigate if the detection of bilobe is due to low Stokes I flux and hence low leakage to V. For this purpose, we have shown CasA image and TauA Stokes V image in Figure 24. The CasA image is at 41 MHz at 22:42 UT on Jan 28, 2025. The TauA image is at 41 MHz at 04:51 MHz on Jan 29, 2025, a few hours later. It is evident that Stokes V bi-lobe is detected at very high significance in case of CasA. The bilobe peaks, while visible in case of TauA, have a SNR smaller than 5. Using the fractional Stokes V in the bilobe in CasA, we estimate that the bilobe should have Stokes V intensity of 62 Jy/beam. The rms in the Stokes V TauA image is only 4 Jy/beam. This implies that the low SNR of TauA bilobe is not because of high rms. This behaviour is noted in multiple other days as well.

Now let us summarize the properties of the Stokes V bilobes:

- **The bilobes observed on a single source is time-variable, which can also be due to apparent motion of the source in the sky**
- **The bilobe orientation need not be same for all sources in the sky at a fixed time and frequency instant.**
- **The bilobe orientation at a fixed time instant and source is similar across frequencies, with the bilobe separation decreasing with increase in frequency.**
- **Presence of bilobe in a source at a given time and frequency slice, does not imply presence of bilobe at other sources.**
- **Presence of bilobes are more likely during the day than at night.**

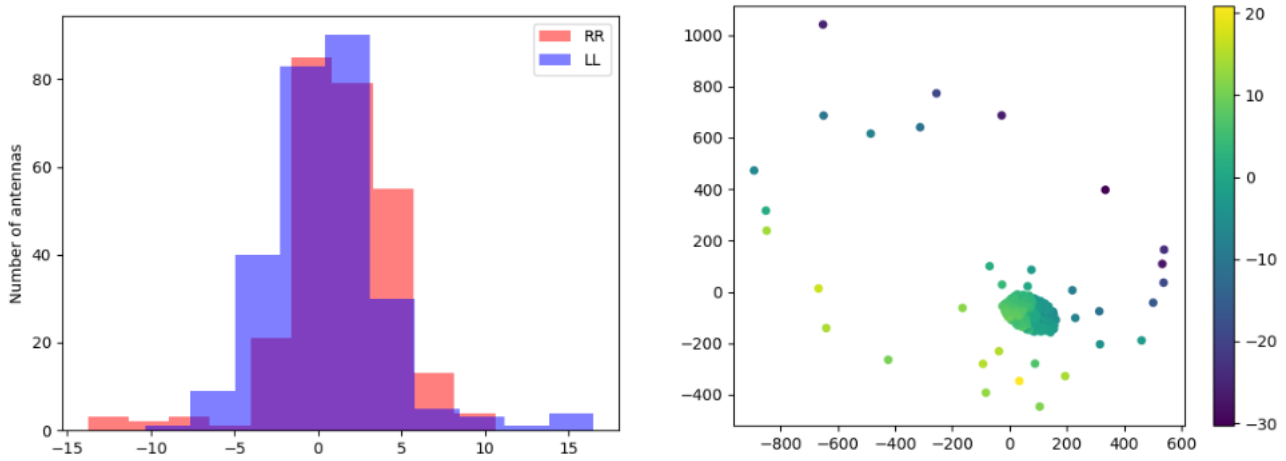

Figure 25: Left panel: Shows the gain phase histogram for the two polarizations. Right panel: Shows the spatial distribution of the difference between antenna gain phases in RL basis.

3.4.4 Possible cause and resolutions

Based on these properties, and reasoning provided in Sections 3.4.1 and 3.4.2, I hypothesize that the bilobes are arising because of birefringent ionospheric refraction of R and L modes through the ionosphere. A possible resolution of this is to convert the calibrated visibilities to RL basis and then do a phase-only selfcal. This procedure will align the RR and LL visibilities. After that, we can transform the visibilities back to the linear basis as was in the original data. In Figure 25 we the gain phases of such a self-calibration test. In the left panel, I show the gain phase histogram for the two polarizations. In the right panel, I color each antenna of the OVRO-LWA array based on the difference of the R and L gain phase. From this figure, we can conclude that the difference is highest for the antennas, which are farthest from the array-centre. I have verified that this procedure does not change any other Stokes images, except removing the bilobe structure of V. Also, while this procedure can correct for sources which have bilobe orientation similar to the strongest source in the sky, if there is any source, whose bi-lobe orientation is different, then it will not get corrected. However, applying this in case of Sun is difficult, because bilobe structures are often expected in case of solar bursts. So judging if the bi-lobes are real or arising due to intrinsic reasons might be difficult. Figure 23 might provide a clue to judging if bilobes are intrinsic or related to this effect. We find that the vast majority of bi-lobes have a separation comparable to the PSF major axis. So if a source has a bi-lobe have separation, greater than twice the major axis, it is very likely to be caused by effects intrinsic to the Sun. However, more thoughts and investigations are needed on this front.

References

Dey Soham, Kansabanik Devojyoti, Oberoi Divya, Mondal Surajit. First Robust Detection of Linear Polarization from Metric Solar Emissions: Challenging Established Paradigms // ApJL. VIII 2025. 988, 2. L73.

Hamaker J. P. Understanding radio polarimetry. IV. The full-coherency analogue of scalar self-calibration: Self-alignment, dynamic range and polarimetric fidelity // A&AS. V 2000. 143. 515–534.

Kansabanik Devojyoti, Vourlidas Angelos, Dey Soham, Mondal Surajit, Oberoi Divya. A Formalism for Calibrating the Instrumental Polarization of Radio Interferometric Arrays at Meter Wavelengths Using Unpolarized Sky: A Demonstration Using MWA Observations // ApJS. V 2025. 278, 1. 26.

Sault R. J., Hamaker J. P., Bregman J. D. Understanding radio polarimetry. II. Instrumental calibration of an interferometer array. // A&AS. V 1996. 117. 149–159.

Appendix

Below, I show figures at all the frequency bands for the A-team sources. These figure format is same as that shown in Figure 9.

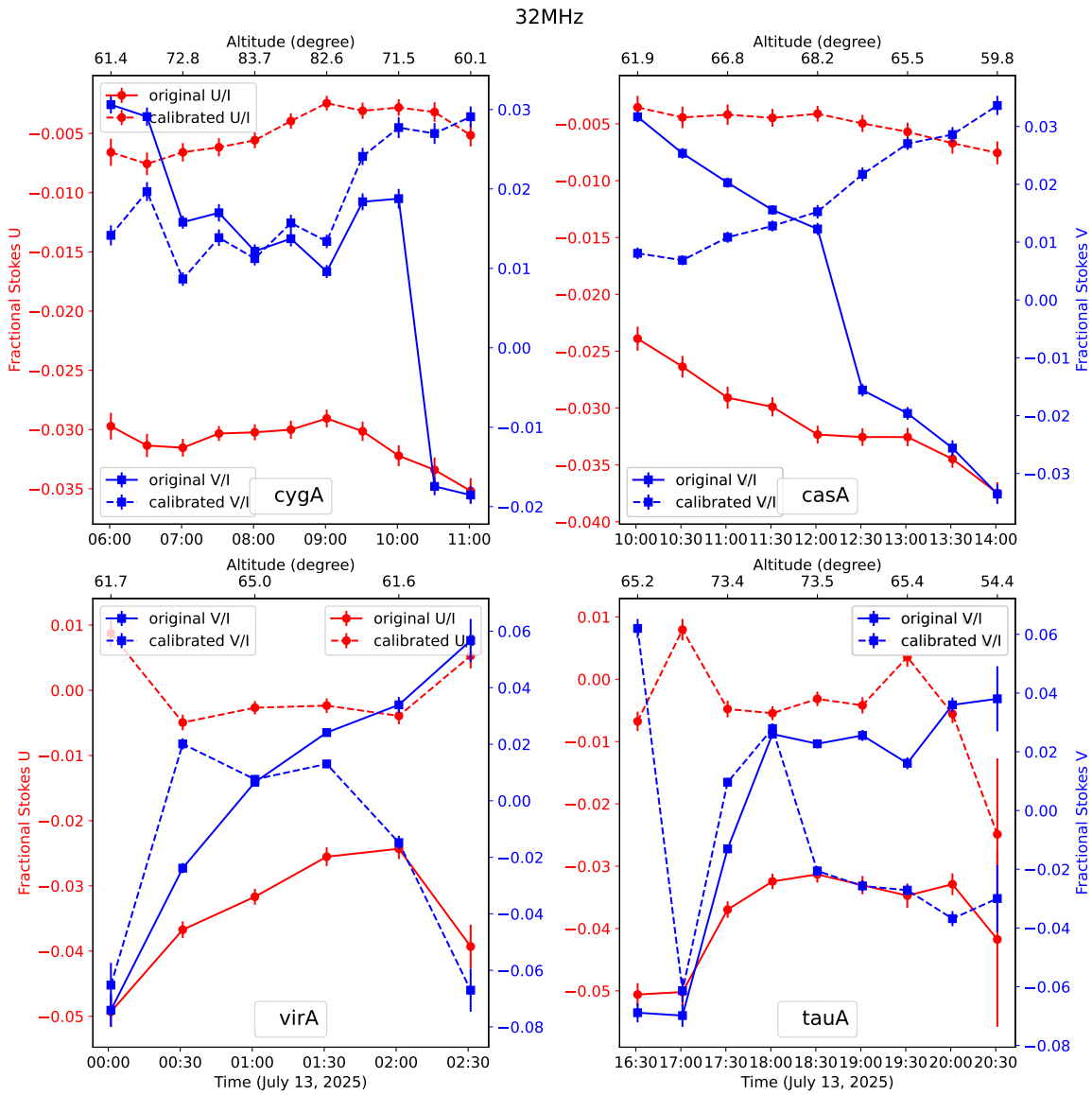
32MHz
Altitude (degree)
61.4 72.8 83.7 82.6 71.5 60.1
61.9 66.8 68.2 65.5 59.8
original U/I
calibrated U/I
original V/I
calibrated V/I
cygA
casA
Fractional Stokes U
Fractional Stokes V
06:00 07:00 08:00 09:00 10:00 11:00
10:00 10:30 11:00 11:30 12:00 12:30 13:00 13:30 14:00
61.7 65.0 61.6
65.2 73.4 73.5 65.4 54.4
original U/I
calibrated U/I
virA
tauA
00:00 00:30 01:00 01:30 02:00 02:30
16:30 17:00 17:30 18:00 18:30 19:00 19:30 20:00 20:30
Time (July 13, 2025)

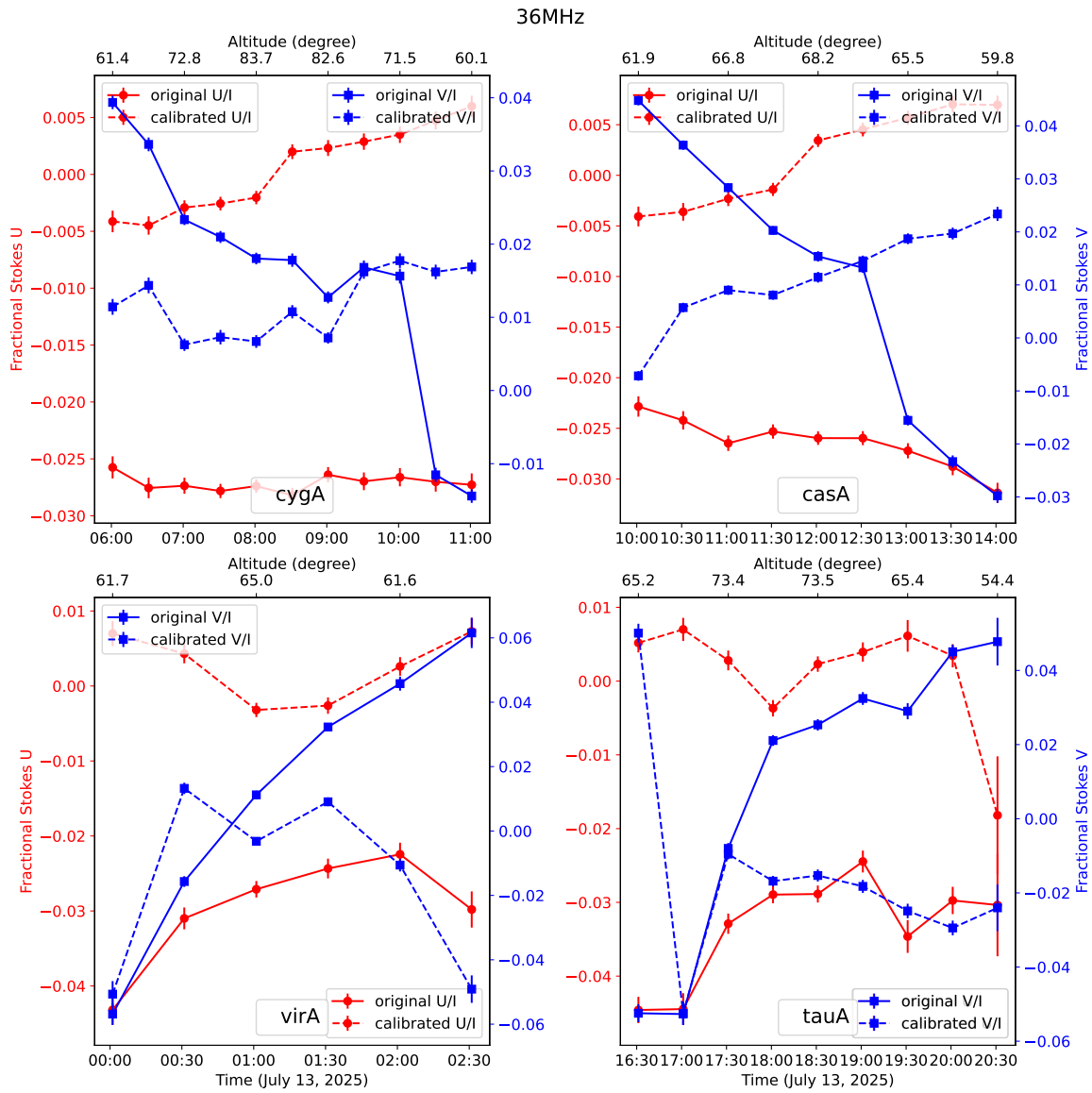
36MHz
Altitude (degree)
61.4 72.8 83.7 82.6 71.5 60.1
61.9 66.8 68.2 65.5 59.8
original U/I
calibrated U/I
original V/I
calibrated V/I
Fractional Stokes U
Fractional Stokes V
cygA
casA
06:00 07:00 08:00 09:00 10:00 11:00
10:00 10:30 11:00 11:30 12:00 12:30 13:00 13:30 14:00
61.7 65.0 61.6
65.2 73.4 73.5 65.4 54.4
virA
tauA
00:00 00:30 01:00 01:30 02:00 02:30
16:30 17:00 17:30 18:00 18:30 19:00 19:30 20:00 20:30
Time (July 13, 2025)

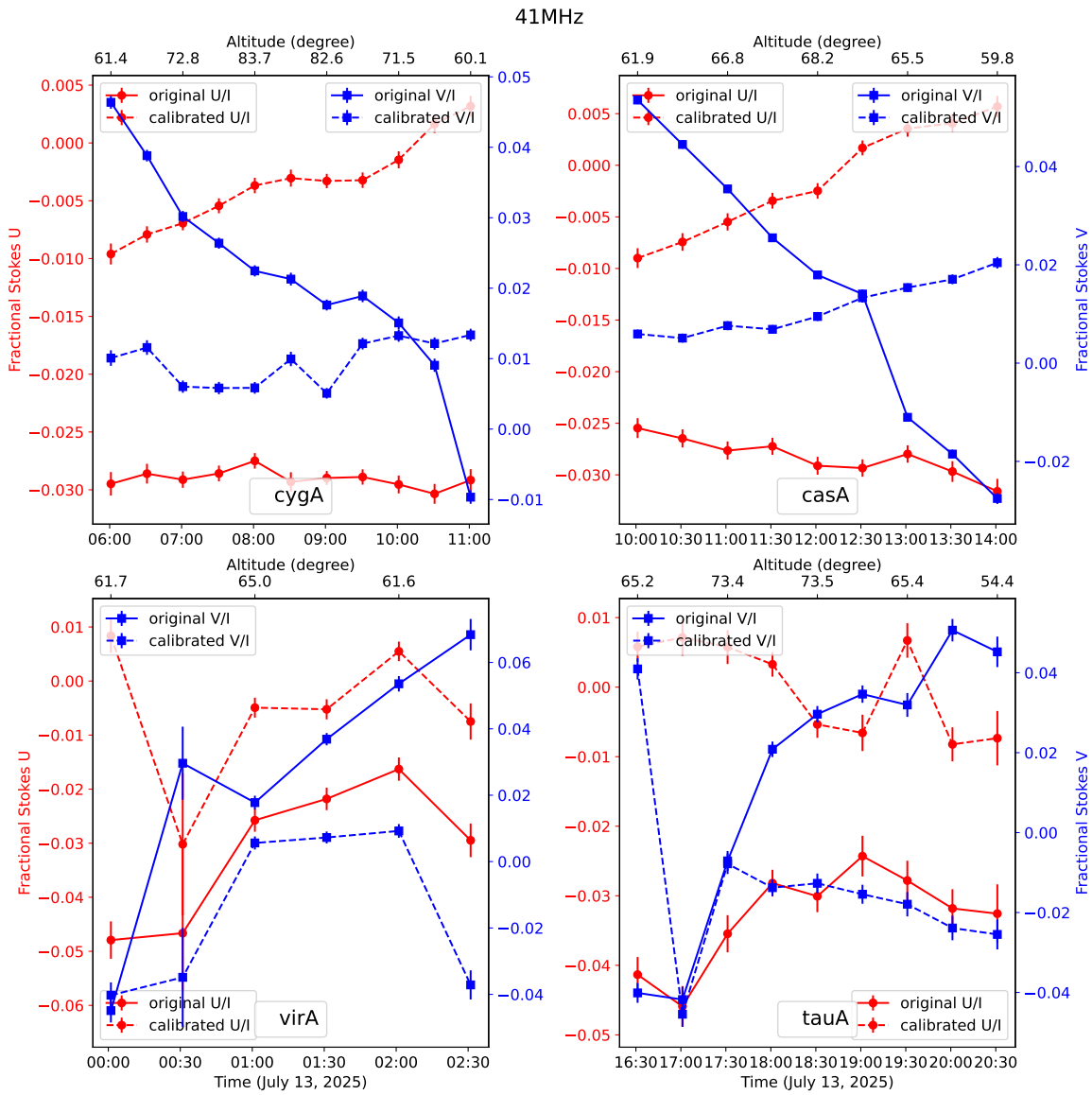
41MHz
Altitude (degree)
61.4 72.8 83.7 82.6 71.5 60.1
61.9 66.8 68.2 65.5 59.8
original U/I
calibrated U/I
original V/I
calibrated V/I
Fractional Stokes U
Fractional Stokes V
cygA
casA
06:00 07:00 08:00 09:00 10:00 11:00
10:00 10:30 11:00 11:30 12:00 12:30 13:00 13:30 14:00
61.7 65.0 61.6
65.2 73.4 73.5 65.4 54.4
virA
tauA
00:00 00:30 01:00 01:30 02:00 02:30
16:30 17:00 17:30 18:00 18:30 19:00 19:30 20:00 20:30
Time (July 13, 2025)

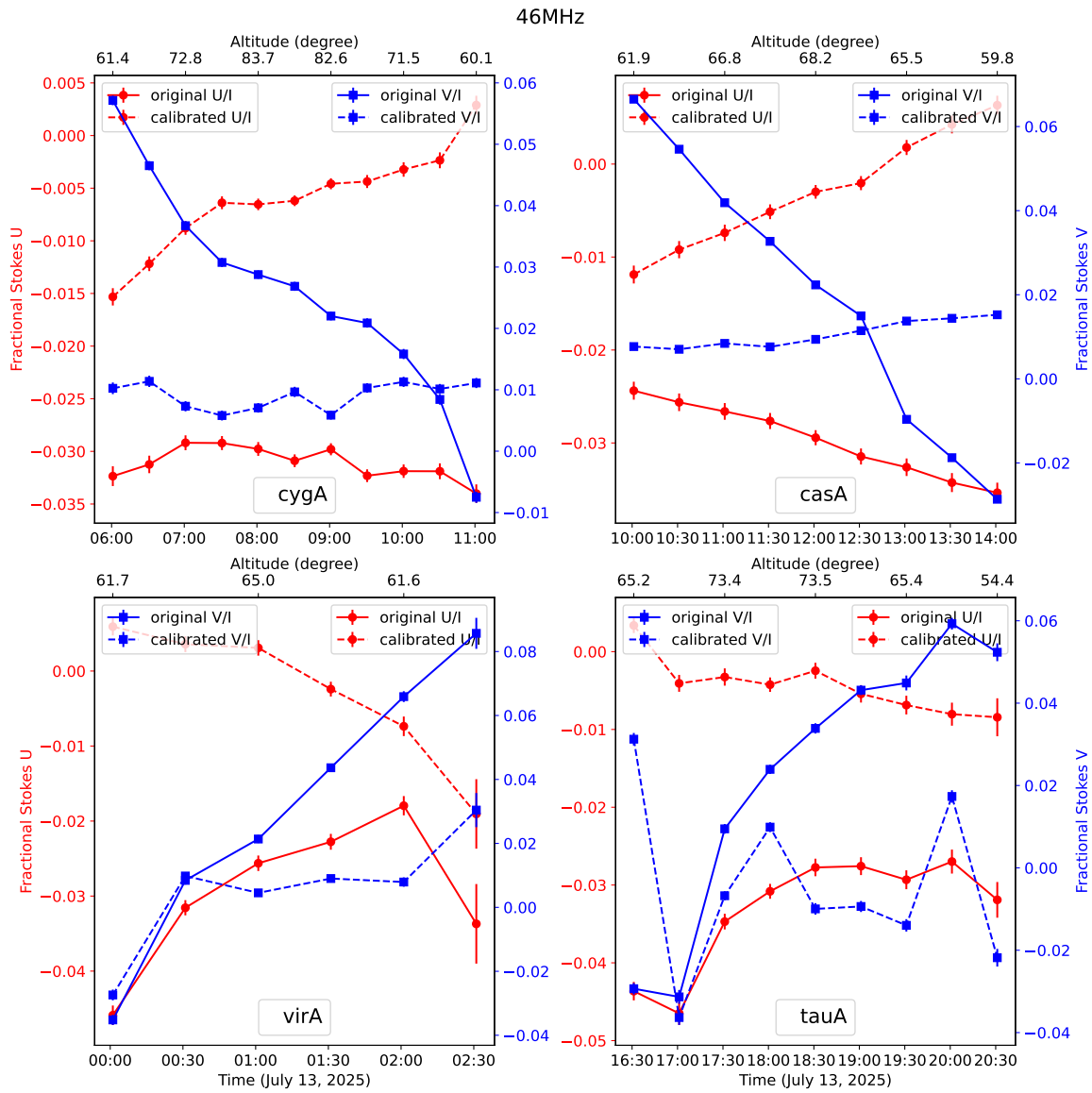
46MHz
Altitude (degree)
61.4 72.8 83.7 82.6 71.5 60.1
61.9 66.8 68.2 65.5 59.8
original U/I
calibrated U/I
original V/I
calibrated V/I
Fractional Stokes U
Fractional Stokes V
cygA
casA
06:00 07:00 08:00 09:00 10:00 11:00
10:00 10:30 11:00 11:30 12:00 12:30 13:00 13:30 14:00
61.7 65.0 61.6
65.2 73.4 73.5 65.4 54.4
virA
tauA
00:00 00:30 01:00 01:30 02:00 02:30
16:30 17:00 17:30 18:00 18:30 19:00 19:30 20:00 20:30
Time (July 13, 2025)

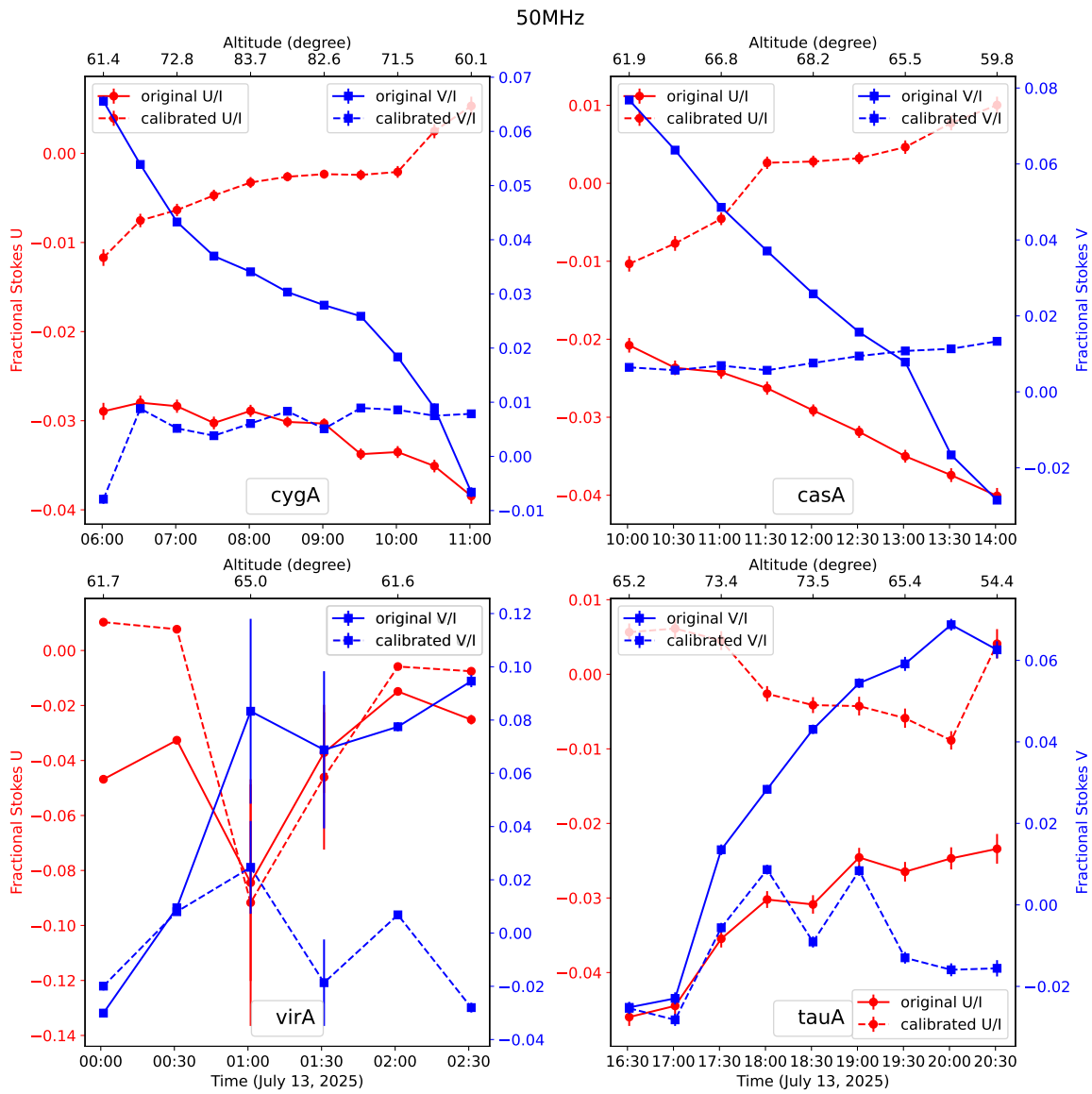
50MHz
Altitude (degree)
61.4 72.8 83.7 82.6 71.5 60.1
61.9 66.8 68.2 65.5 59.8
original U/I
calibrated U/I
original V/I
calibrated V/I
Fractional Stokes U
Fractional Stokes V
cygA
casA
06:00 07:00 08:00 09:00 10:00 11:00
10:00 10:30 11:00 11:30 12:00 12:30 13:00 13:30 14:00
61.7 65.0 61.6
65.2 73.4 73.5 65.4 54.4
virA
tauA
00:00 00:30 01:00 01:30 02:00 02:30
16:30 17:00 17:30 18:00 18:30 19:00 19:30 20:00 20:30
Time (July 13, 2025)

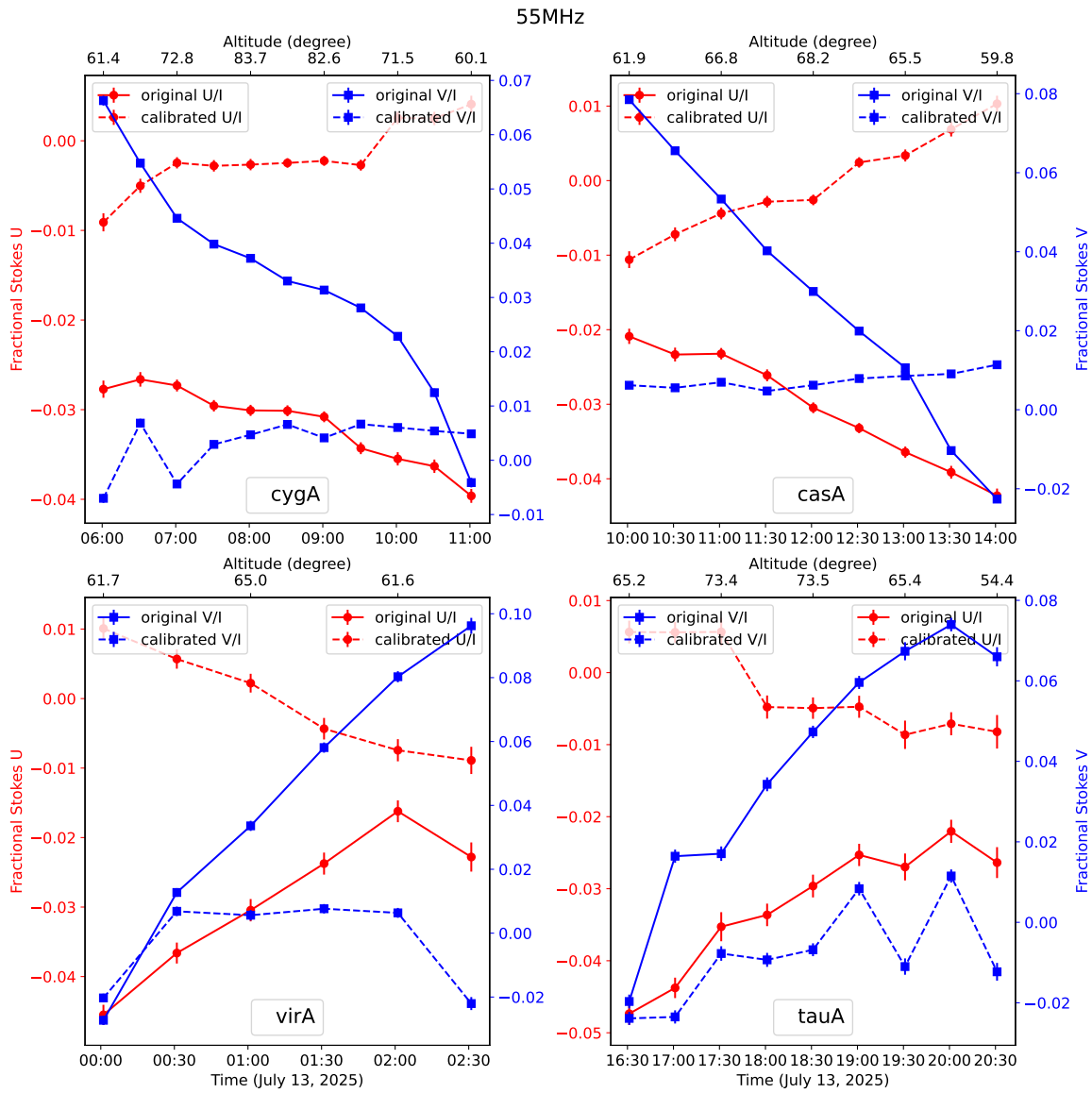
55MHz
Altitude (degree)
61.4 72.8 83.7 82.6 71.5 60.1
61.9 66.8 68.2 65.5 59.8
original U/I
calibrated U/I
original V/I
calibrated V/I
Fractional Stokes U
Fractional Stokes V
cygA
casA
06:00 07:00 08:00 09:00 10:00 11:00
10:00 10:30 11:00 11:30 12:00 12:30 13:00 13:30 14:00
61.7 65.0 61.6
65.2 73.4 73.5 65.4 54.4
virA
tauA
00:00 00:30 01:00 01:30 02:00 02:30
16:30 17:00 17:30 18:00 18:30 19:00 19:30 20:00 20:30
Time (July 13, 2025)

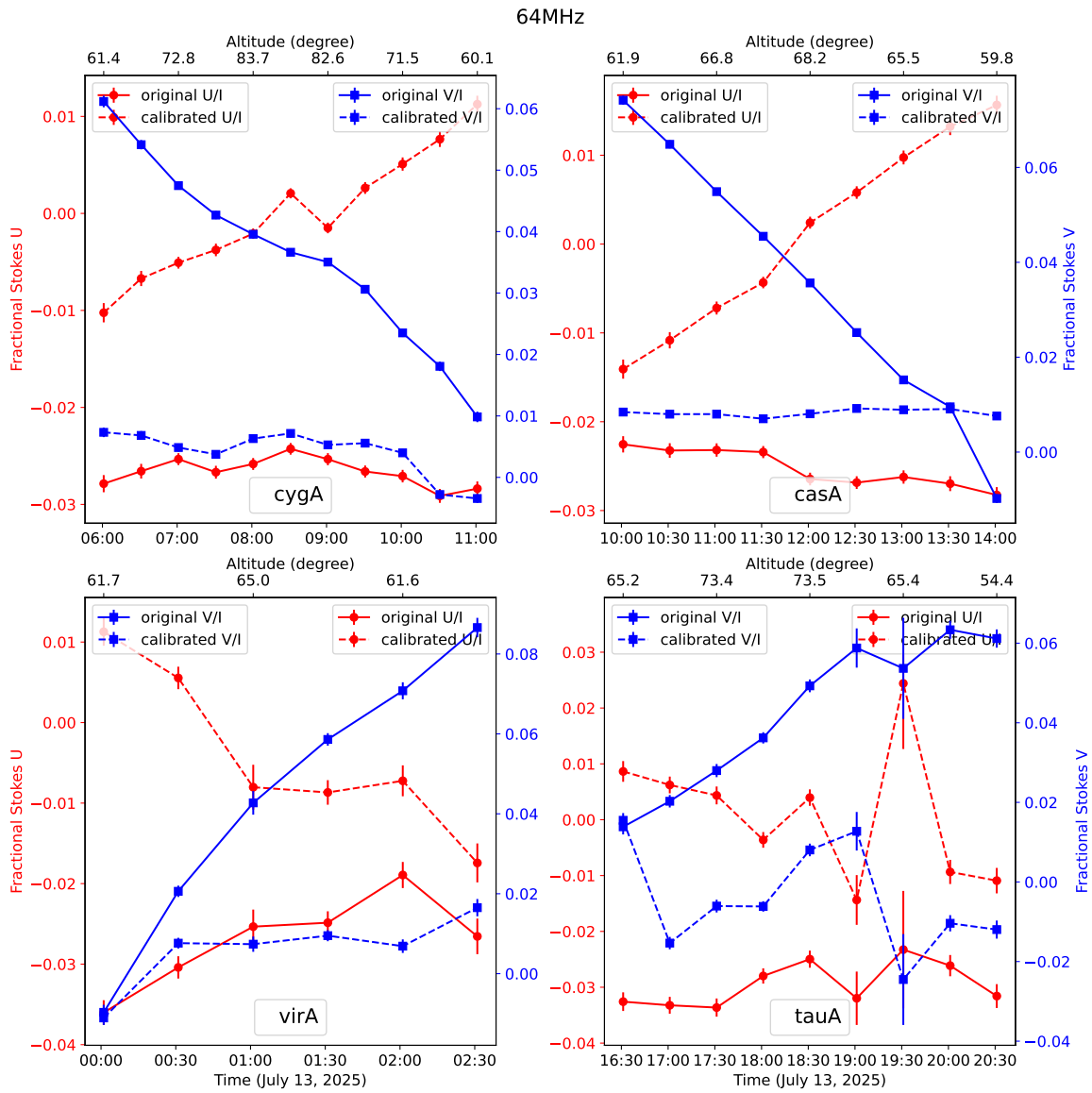
64MHz
Altitude (degree)
61.4 72.8 83.7 82.6 71.5 60.1
original U/I
calibrated U/I
original V/I
calibrated V/I
Fractional Stokes U
Fractional Stokes V
cygA
06:00 07:00 08:00 09:00 10:00 11:00
Altitude (degree)
61.9 66.8 68.2 65.5 59.8
casA
10:00 10:30 11:00 11:30 12:00 12:30 13:00 13:30 14:00
Altitude (degree)
61.7 65.0 61.6
virA
00:00 00:30 01:00 01:30 02:00 02:30
Time (July 13, 2025)
Altitude (degree)
65.2 73.4 73.5 65.4 54.4
tauA
16:30 17:00 17:30 18:00 18:30 19:00 19:30 20:00 20:30
Time (July 13, 2025)

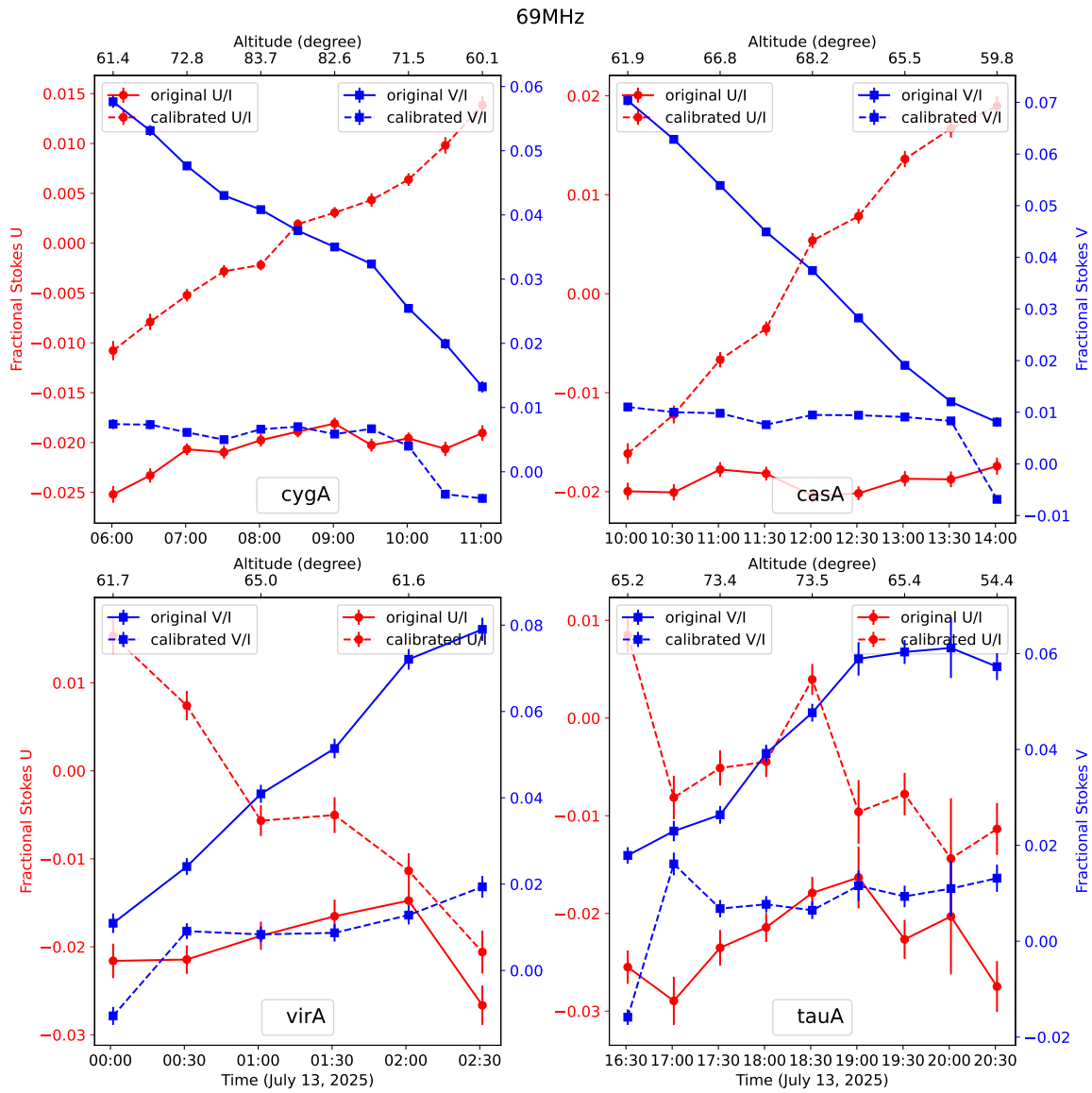
69MHz
Altitude (degree)
61.4 72.8 83.7 82.6 71.5 60.1
61.9 66.8 68.2 65.5 59.8
original U/I
calibrated U/I
original V/I
calibrated V/I
Fractional Stokes U
Fractional Stokes V
cygA
casA
06:00 07:00 08:00 09:00 10:00 11:00
10:00 10:30 11:00 11:30 12:00 12:30 13:00 13:30 14:00
61.7 65.0 61.6
65.2 73.4 73.5 65.4 54.4
virA
tauA
00:00 00:30 01:00 01:30 02:00 02:30
16:30 17:00 17:30 18:00 18:30 19:00 19:30 20:00 20:30
Time (July 13, 2025)

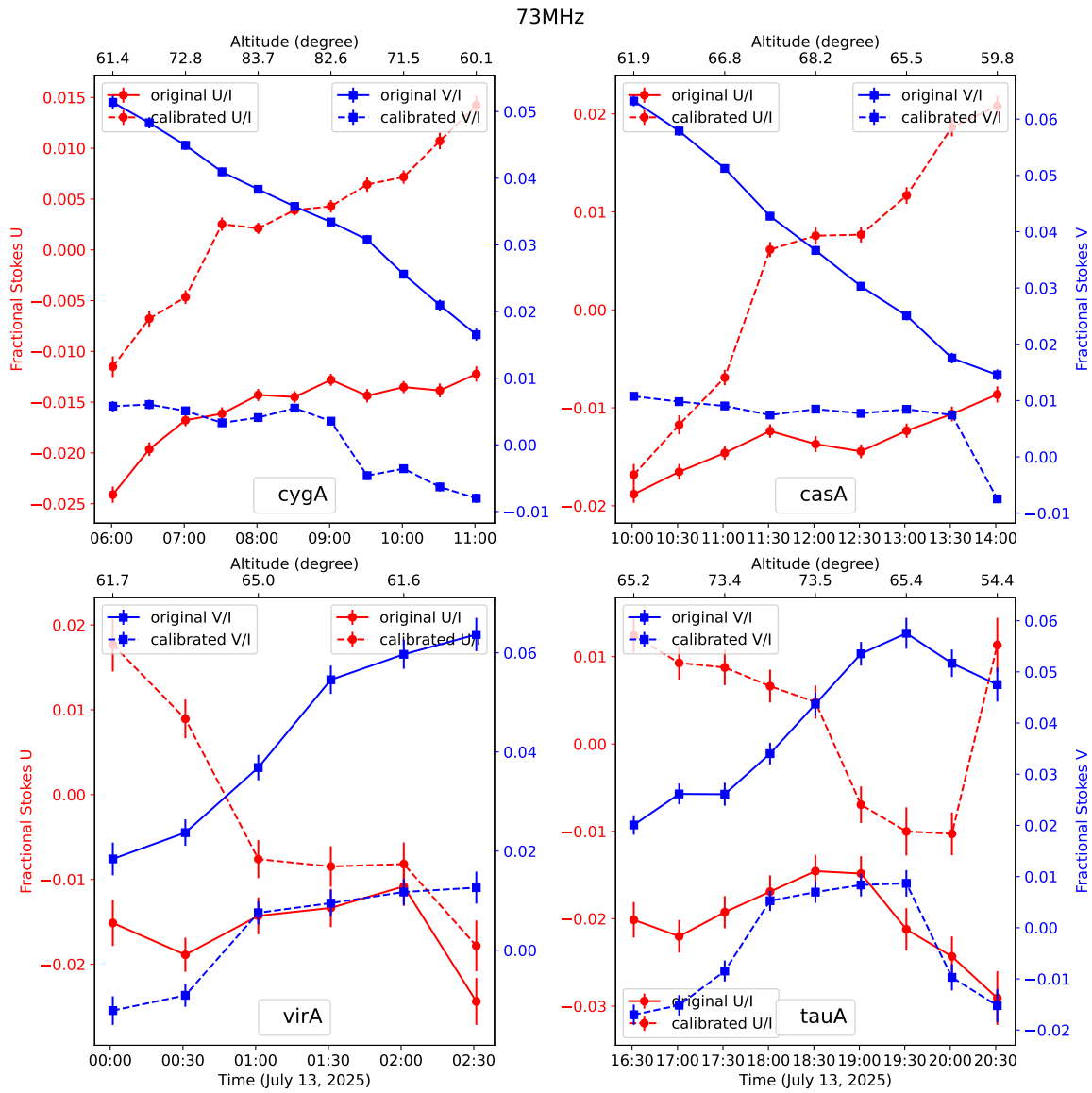
73MHz
Altitude (degree)
61.4 72.8 83.7 82.6 71.5 60.1
61.9 66.8 68.2 65.5 59.8
61.7 65.0 61.6
65.2 73.4 73.5 65.4 54.4
original U/I
calibrated U/I
original V/I
calibrated V/I
Fractional Stokes U
Fractional Stokes V
cygA
casA
virA
tauA
06:00 07:00 08:00 09:00 10:00 11:00
10:00 10:30 11:00 11:30 12:00 12:30 13:00 13:30 14:00
00:00 00:30 01:00 01:30 02:00 02:30
16:30 17:00 17:30 18:00 18:30 19:00 19:30 20:00 20:30
Time (July 13, 2025)

78MHz

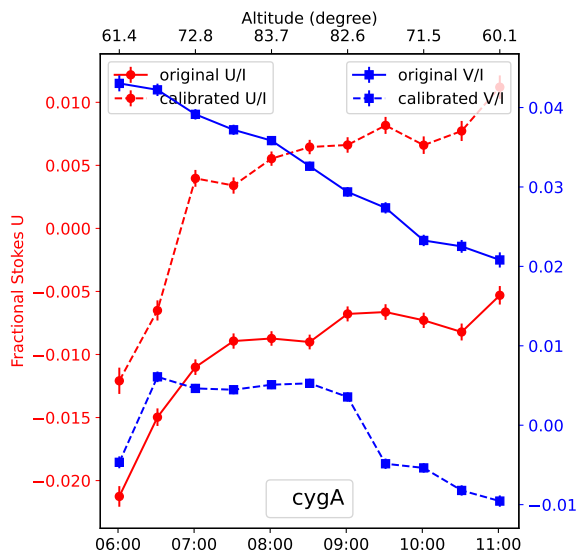
Altitude (degree)
61.4
72.8
83.7
82.6
71.5
60.1
original U/I
calibrated U/I
original V/I
calibrated V/I
Fractional Stokes U
Fractional Stokes V
cygA
06:00
07:00
08:00
09:00
10:00
11:00

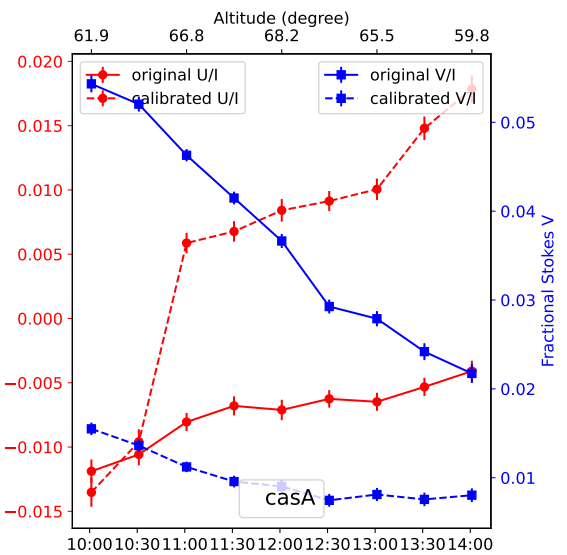
Altitude (degree)
61.9
66.8
68.2
65.5
59.8
original U/I
calibrated U/I
original V/I
calibrated V/I
Fractional Stokes V
casA
10:00
10:30
11:00
11:30
12:00
12:30
13:00
13:30
14:00

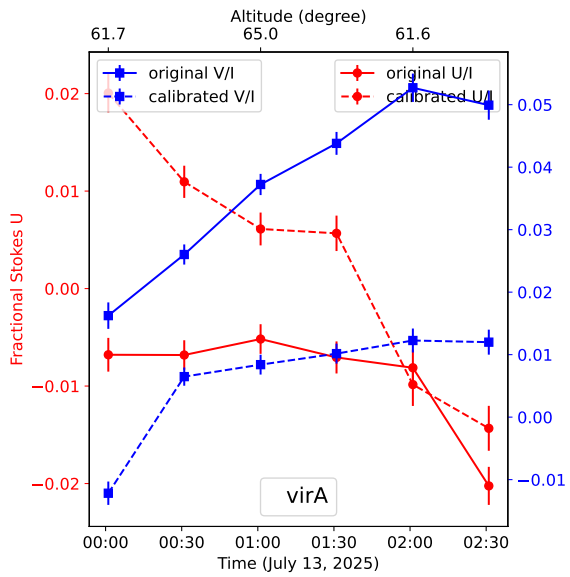
Altitude (degree)
61.7
65.0
61.6
original V/I
calibrated V/I
original U/I
calibrated U/I
Fractional Stokes U
virA
00:00
00:30
01:00
01:30
02:00
02:30
Time (July 13, 2025)

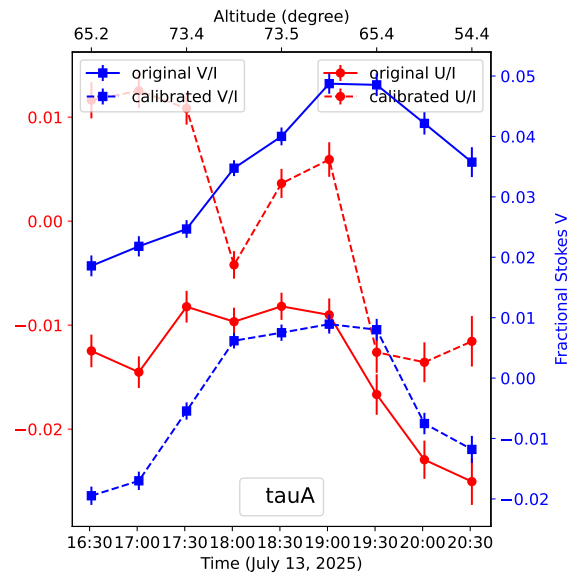
Altitude (degree)
65.2
73.4
73.5
65.4
54.4
original V/I
calibrated V/I
original U/I
calibrated U/I
Fractional Stokes V
tauA
16:30
17:00
17:30
18:00
18:30
19:00
19:30
20:00
20:30
Time (July 13, 2025)

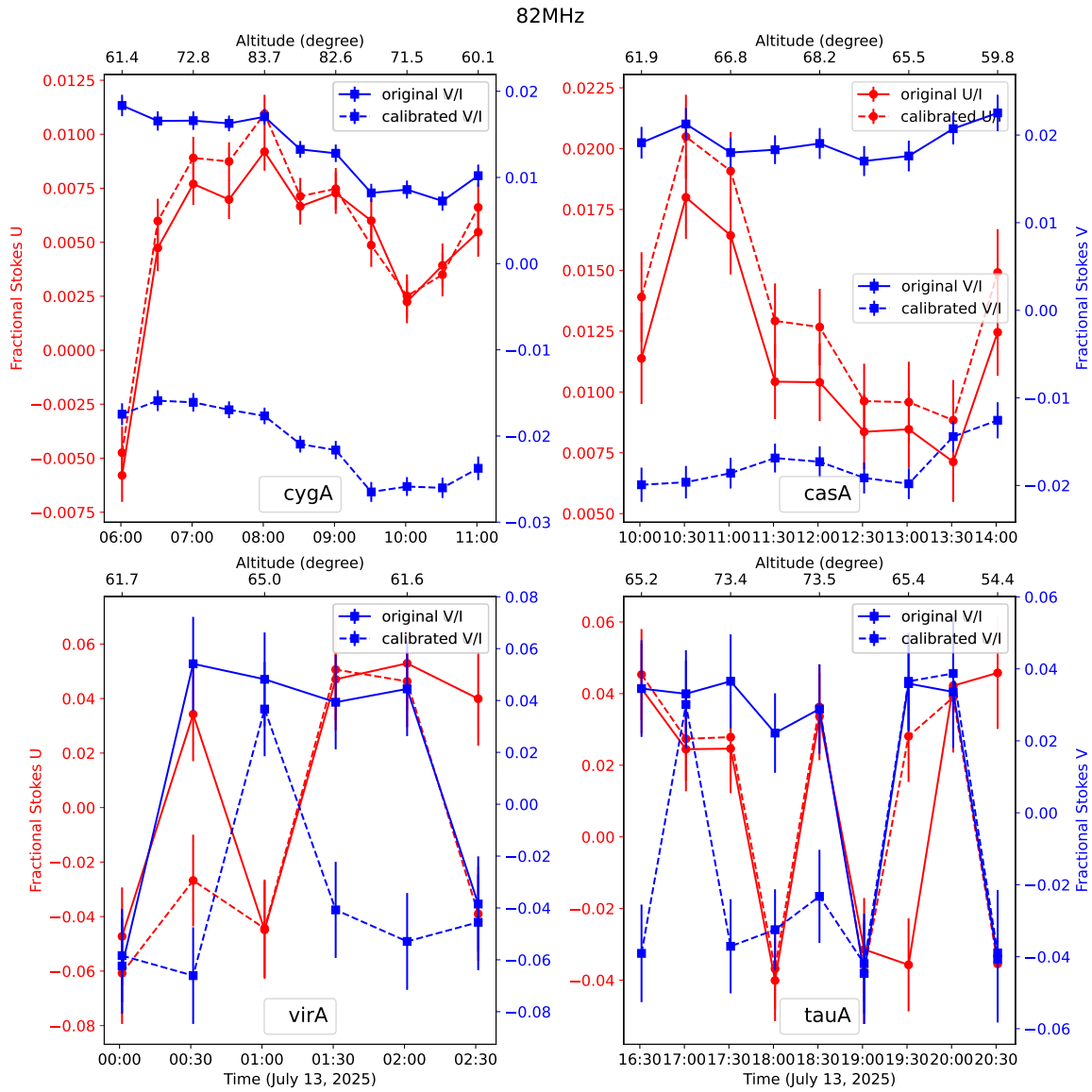
82MHz
Altitude (degree)
61.4 72.8 83.7 82.6 71.5 60.1
61.9 66.8 68.2 65.5 59.8
original V/I
calibrated V/I
original U/I
calibrated U/I
Fractional Stokes U
Fractional Stokes V
cygA
casA
06:00 07:00 08:00 09:00 10:00 11:00
10:00 10:30 11:00 11:30 12:00 12:30 13:00 13:30 14:00
61.7 65.0 61.6
65.2 73.4 73.5 65.4 54.4
virA
tauA
00:00 00:30 01:00 01:30 02:00 02:30
16:30 17:00 17:30 18:00 18:30 19:00 19:30 20:00 20:30
Time (July 13, 2025)

We find that while at frequencies, and all sources, the variation of observed polarization fraction has decreased, at lower frequencies, the absolute polarization fraction observed is higher than that at the higher frequencies. We also find that VirA and TauA show higher variability and also higher polarization fraction. In Figure 26 we show the CasA U and V images at 32MHz similar to bottom panels of Figure 9. During time time, the elevation of CasA was about 61°. Note that this is deep in the night of California. Sun has set hours ago. We find that even at the lowest frequency, before polarization calibration, the Stokes V fraction is high, not bi-lobe is not present. After calibration, we however, see the bi-lobe structure, albeit at much lower residual polarization fraction. However, at daytime, the bi-lobes becomes much more dominant. In Figure 27 we show the U and V images of TauA at 69MHz, again when it had similar elevation as CasA in Figure 26. It is evident that even at 69 MHz, before any calibration, we see the bi-lobes. Polarization calibration, done here, is not designed to remove the bi-lobes and hence as expected has not removed it. Bi-lobes are present at the exact same level before and after calibration. Stokes U, however, has decreased significantly after calibration. It should also be noted that during this time, it was daytime in California. This again suggests that there is a day-night difference in the bi-lobe structure

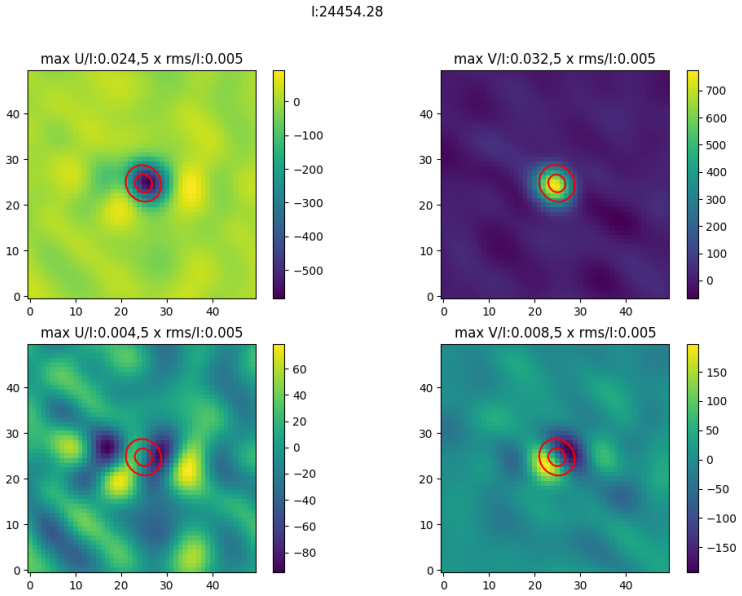

Figure 26: CasA U and V images at 32–37 MHz, 10:01 UT on July 13, 2025. Image format is same is as in bottom panels of Figure 9.

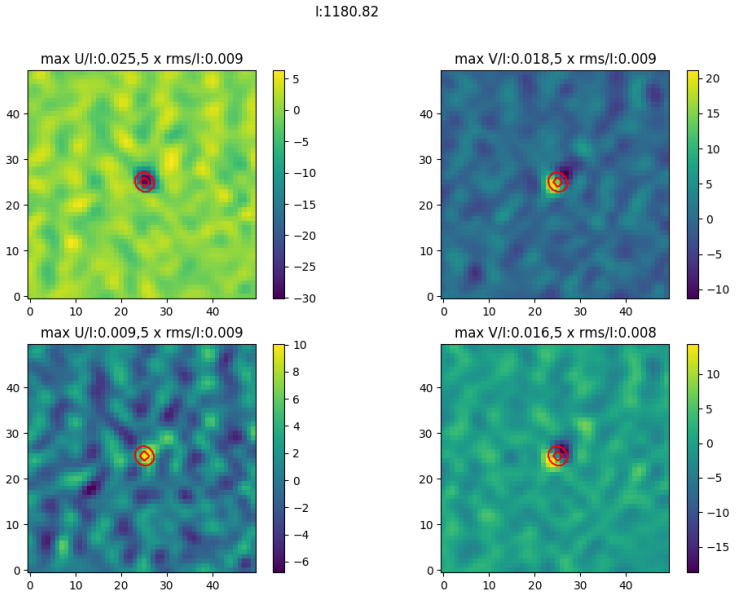

Figure 27: TauA U and V images at 69–73 MHz, 16:31 UT on July 13, 2025. Image format is same is as in bottom panels of Figure 9.

Next, we also show the Stokes U and V images in same format for TauA between Jan 20 – Feb 14, 2025, at 55MHz.

To not overwhelm the reader, we have randomly chosen a few dates and shown them here. Note that the solutions were determined on January 28, 2025, using data when CygA was above 60° elevation. We chose to show TauA, because it was imaged deep in local night and hence was highly suited for judging the quality of polarization calibration and the stability of the solutions. Each image below corresponds to a particular day, close to transit of TauA. The images prove that the solutions are quite stable and have decreased Stokes U and V significantly in all the timeslices imaged. Similar results are seen in other frequencies as well.

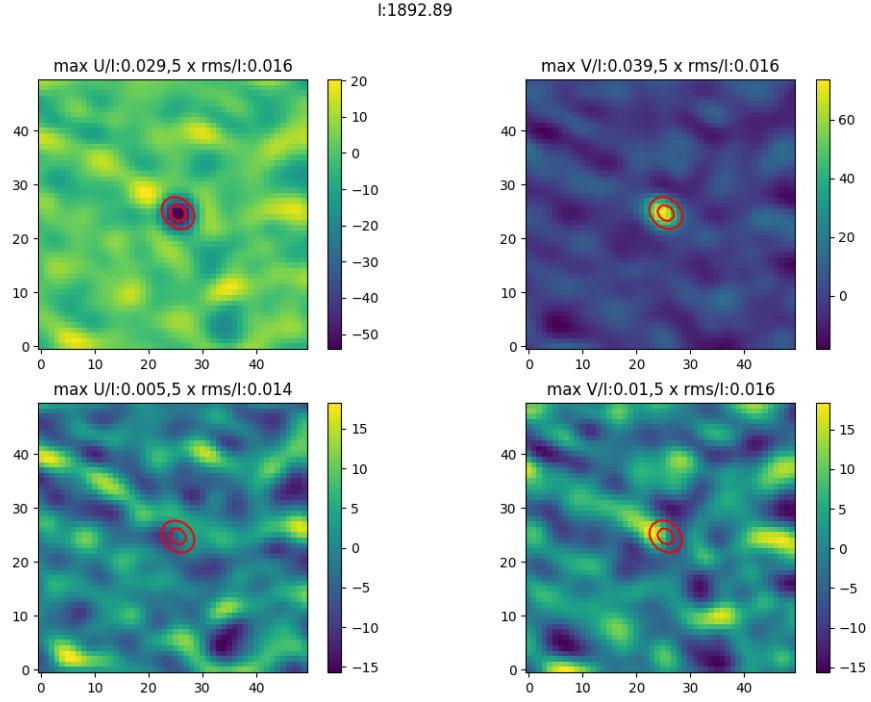
I:1892.89
max U/I:0.029,5 x rms/I:0.016
max V/I:0.039,5 x rms/I:0.016
max U/I:0.005,5 x rms/I:0.014
max V/I:0.01,5 x rms/I:0.016

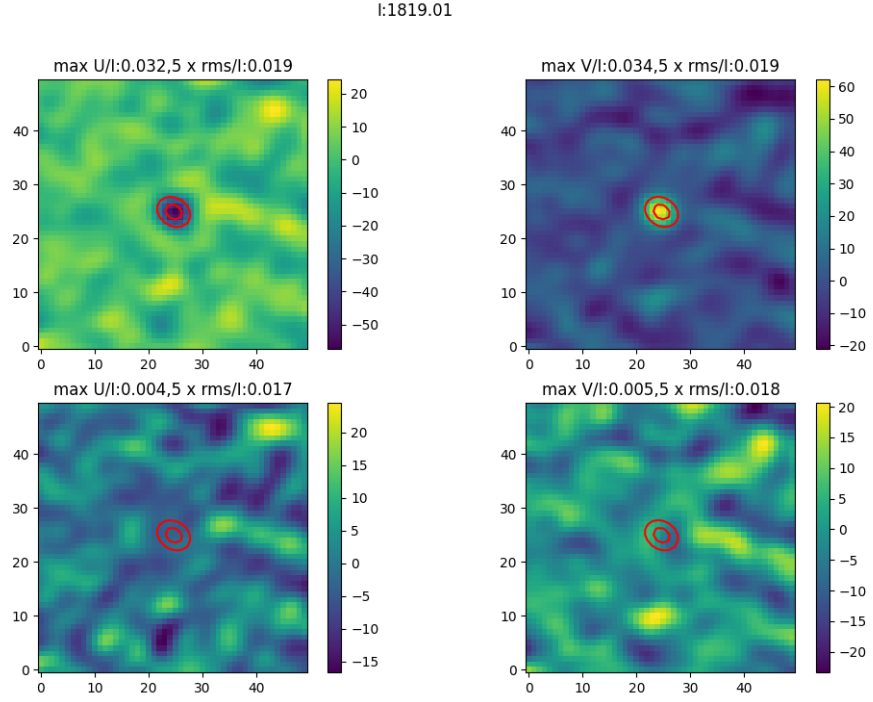
I:1819.01
max U/I:0.032,5 x rms/I:0.019
max V/I:0.034,5 x rms/I:0.019
max U/I:0.004,5 x rms/I:0.017
max V/I:0.005,5 x rms/I:0.018

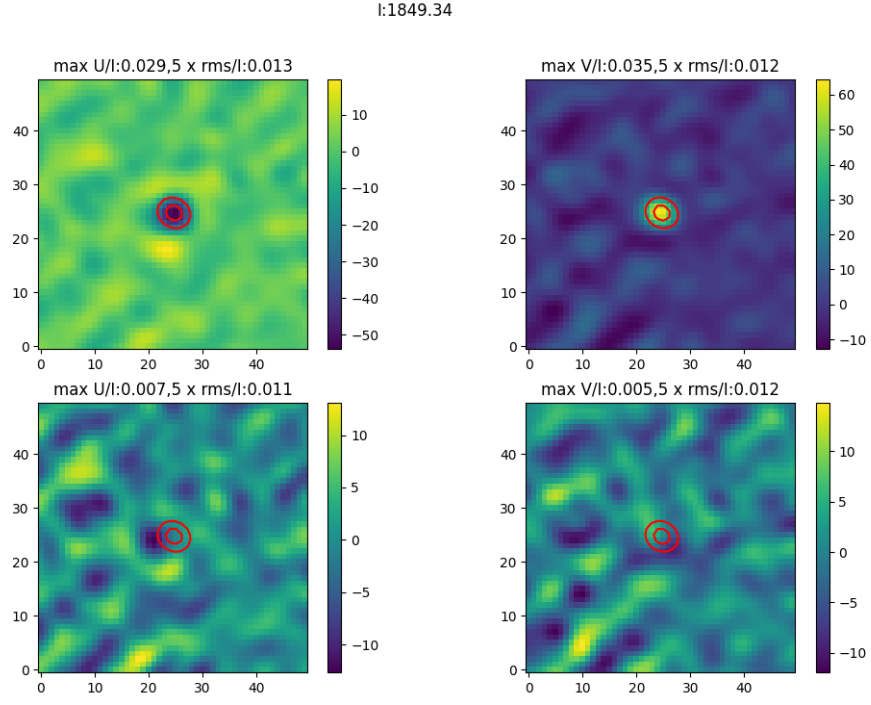
I:1849.34
max U/I:0.029,5 x rms/I:0.013
max V/I:0.035,5 x rms/I:0.012
max U/I:0.007,5 x rms/I:0.011
max V/I:0.005,5 x rms/I:0.012

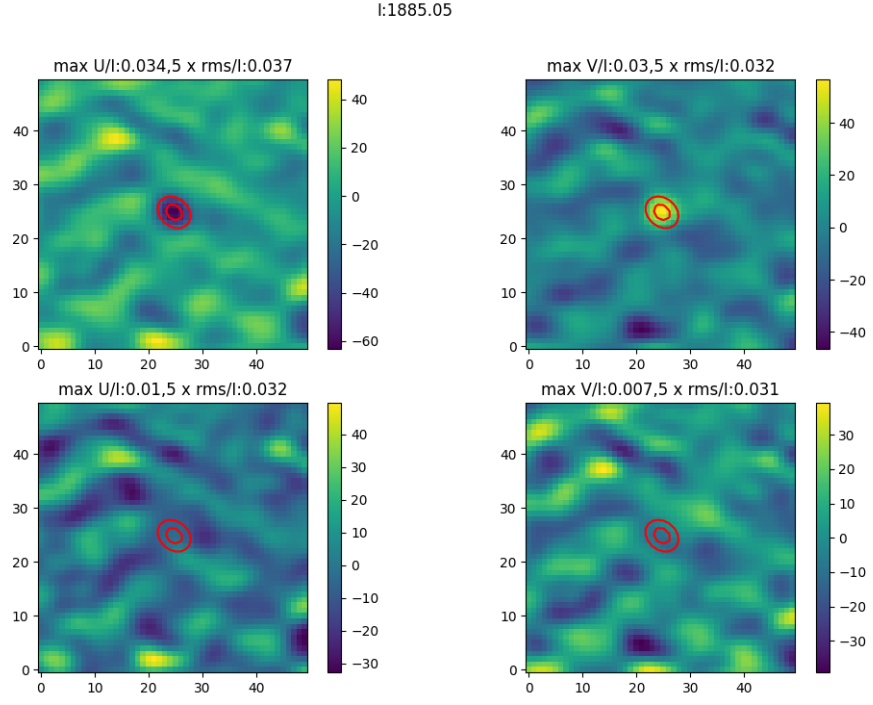
I:1885.05
max U/I:0.034,5 x rms/I:0.037
max V/I:0.03,5 x rms/I:0.032
max U/I:0.01,5 x rms/I:0.032
max V/I:0.007,5 x rms/I:0.031

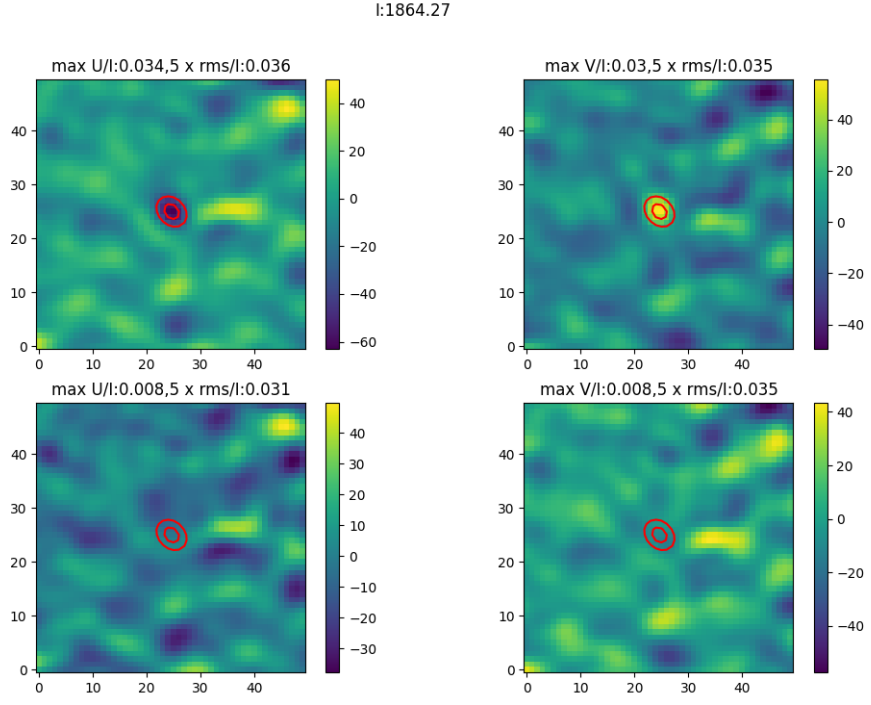
I:1864.27
max U/I:0.034,5 x rms/I:0.036
max V/I:0.03,5 x rms/I:0.035
max U/I:0.008,5 x rms/I:0.031
max V/I:0.008,5 x rms/I:0.035

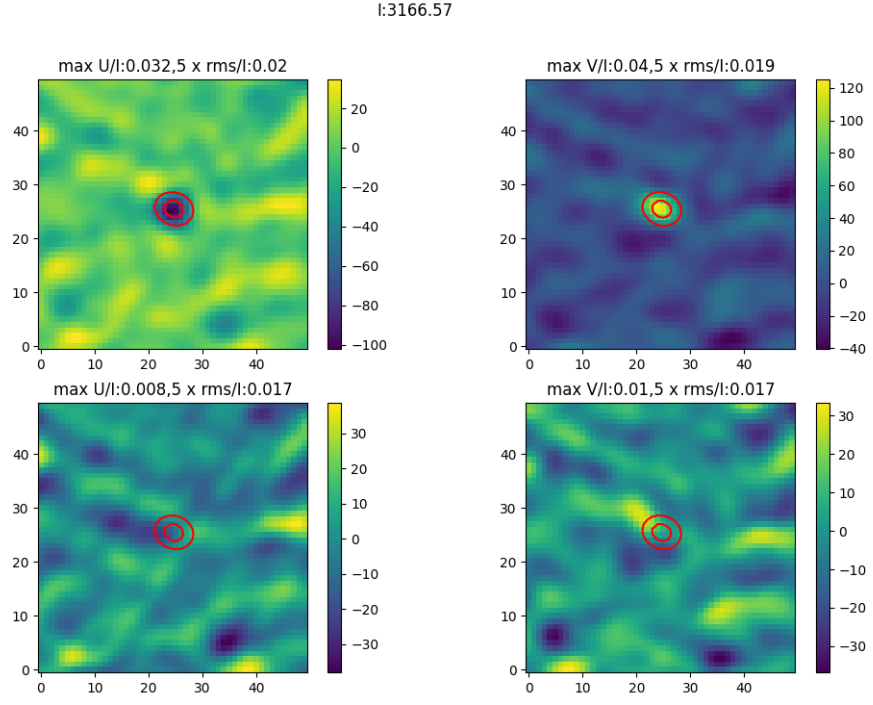
I:3166.57
max U/I:0.032,5 x rms/I:0.02
max V/I:0.04,5 x rms/I:0.019
max U/I:0.008,5 x rms/I:0.017
max V/I:0.01,5 x rms/I:0.017

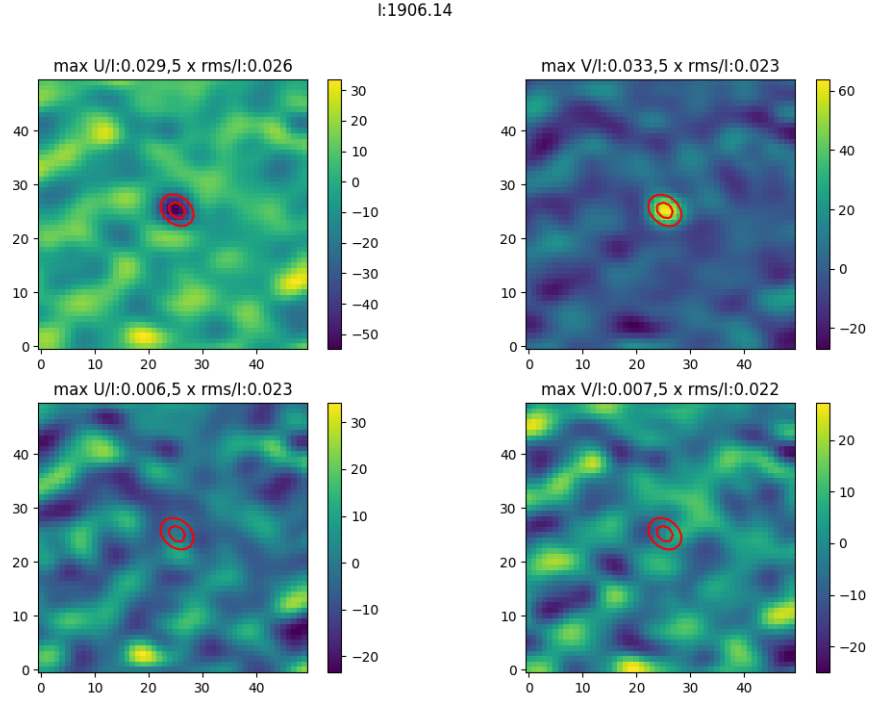
I:1906.14
max U/I:0.029,5 x rms/I:0.026
max V/I:0.033,5 x rms/I:0.023
max U/I:0.006,5 x rms/I:0.023
max V/I:0.007,5 x rms/I:0.022

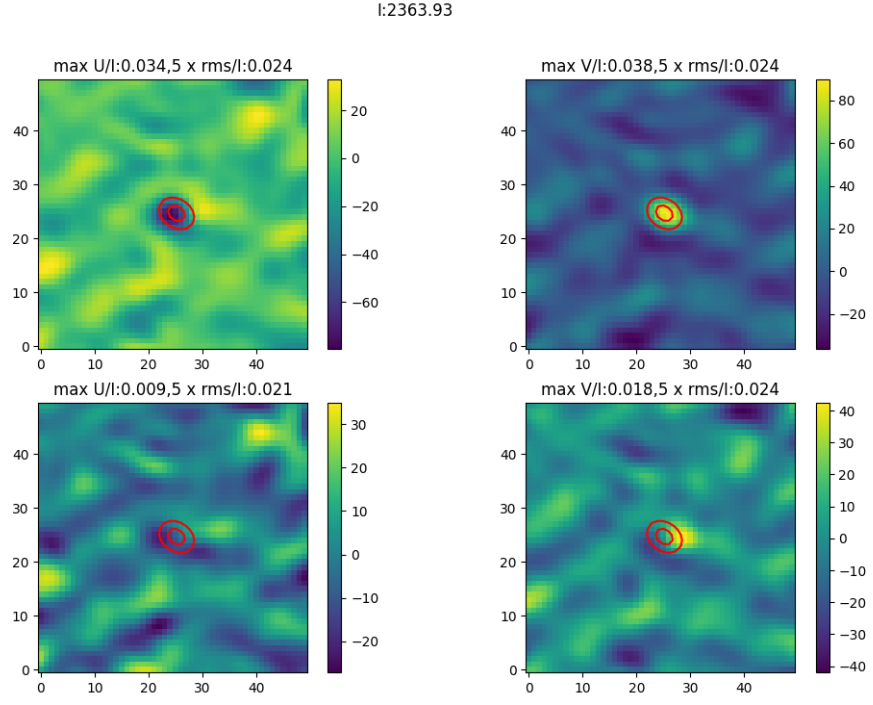
I:2363.93
max U/I:0.034,5 x rms/I:0.024
max V/I:0.038,5 x rms/I:0.024
max U/I:0.009,5 x rms/I:0.021
max V/I:0.018,5 x rms/I:0.024

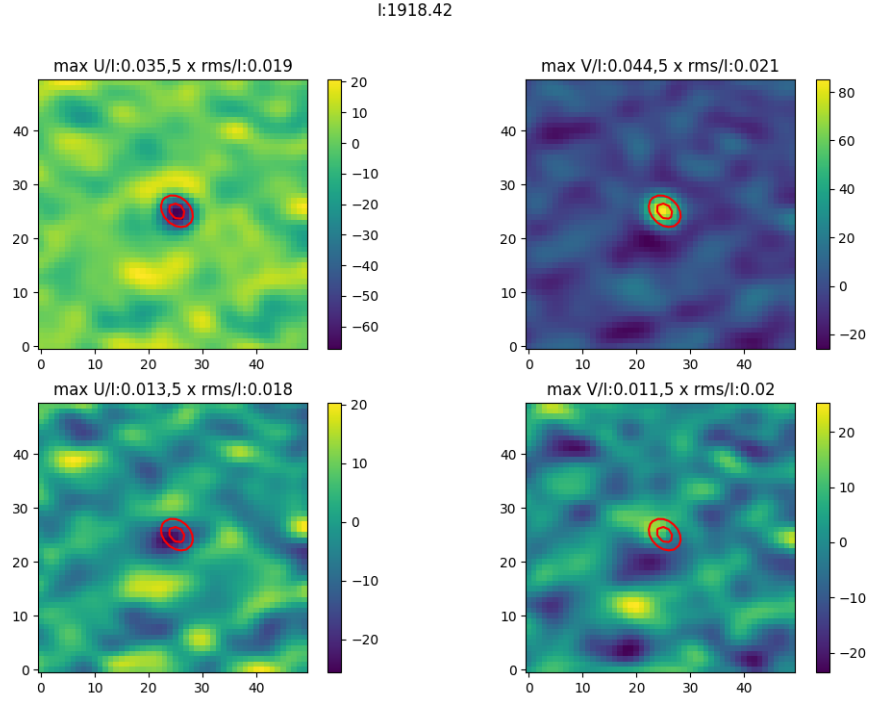
I:1918.42
max U/I:0.035,5 x rms/I:0.019
max V/I:0.044,5 x rms/I:0.021
max U/I:0.013,5 x rms/I:0.018
max V/I:0.011,5 x rms/I:0.02